J. Mech. Phys. Solids 208 (2026) 106467

Contents lists available at ScienceDirect

Journal of the Mechanics and Physics of Solids

journal homepage: www.elsevier.com/locate/jmps

Shell-lattice metamaterials with intrinsic contact stabilization for exceptional mechanical performance and nonlinear stability

Peijie Zhang [a], Xueyan Chen [a,*], Penghui Yu [a], Kun Zhao [b], Hang Yin [a], Changguo Wang [a], Huifeng Tan [a], Muamer Kadic [c]

[a] National Key Laboratory of Science and Technology on Advanced Composites in Special Environments, Harbin Institute of Technology, 92 Xidazhi Street, Harbin, 150001, PR China
[b] Hunan Saidret Space Technology, 1288 Yunlong Road, Hunan, 412000, PR China
[c] Université Marie et Louis Pasteur, SUPMICROTECH, Institut FEMTO-ST, 25000 Besançon, France

ARTICLE INFO

Keywords:
Mechanical metamaterials
Energy absorption
Stretching-dominated
Contact compensation mechanism
Stable plateau stress

ABSTRACT

Although lattice mechanical metamaterials offer low weight and tailorable properties, they face a fundamental barrier to adoption at low relative densities: optimising elastic-plastic performance usually results in reduced buckling resistance (nonlinear stability). Here, we present a novel shell-lattice metamaterial design methodology that eliminates the need to compromise between high yield strength and nonlinear stability at low relative densities. This methodology also provides high specific stiffness and high energy absorption. Our design features seamlessly integrated elliptical hollow struts and hollow spherical nodes. Leveraging a stretching-dominated mechanism augmented by contact-enhanced stabilisation, the architecture provides compensatory reinforcement under large deformations. We numerically investigate and experimentally validate the influence of key geometrical ratios on the mechanical properties. Crucially, elastic isotropy can be achieved through parameter optimisation, and broad tenability enables customised anisotropic elastic responses for diverse applications. Across relative densities ranging from 0.01 to 0.5, our proposed shell lattices demonstrate consistent superiority over conventional truss and shell lattices of equal density. At a relative density of 0.1, the designs deliver a 5 % rise in Young's modulus, a 38 % increase in yield strength, and almost double the energy absorption capacity, significantly outperforming conventional TPMS-like shell lattices. These enhancements arise from internal contact mechanisms that stabilise post-buckling behaviour, yielding consistent or enhanced stress-strain responses. This methodology overcomes the limitations of low-density stretching-dominated lattices, paving the way for advanced, lightweight, load-bearing structures, energy absorbers, and multifunctional metamaterials.

1. Introduction

Driven by rapid advances in additive manufacturing and the escalating need for high-performance materials, modern engineering has increasingly focused on lightweight multifunctional materials that combine low weight with exceptional mechanical properties

* Corresponding author.
E-mail addresses: qiuzhuzpj@163.com (P. Zhang), chenxueyan@hit.edu.cn (X. Chen), 22B918013@stu.hit.edu.cn (P. Yu), 18731263052@163.com (K. Zhao), 630874880@qq.com (H. Yin), wangcg@hit.edu.cn (C. Wang), tanhf@hit.edu.cn (H. Tan), muamer.kadic@femto-st.fr (M. Kadic).

https://doi.org/10.1016/j.jmps.2025.106467
Received 17 October 2025; Received in revised form 27 November 2025; Accepted 1 December 2025
Available online 4 December 2025
0022-5096/© 2025 Elsevier Ltd. All rights are reserved, including those for text and data mining, AI training, and similar technologies.

(Chen et al., 2020, 2022; Tan et al., 2022; Milton et al., 2017). Mechanical metamaterials satisfy these stringent criteria by precisely tuning mechanical responses through the reconfiguration of complex geometries (Chen et al., 2024; Li et al., 2018; Abbasi et al., 2024; Dudek et al., 2025a).Tailored architectures unlock a spectrum of functionalities, including low density (Zhang et al., 2025, 2023; Poincloux et al., 2023),acoustic absorption (Li et al., 2021c,b),programmable morphing (Zhu et al., 2024; Chen et al., 2021; Jin et al., 2025), tunable Poisson's ratios (Yu et al., 2024; Tan et al., 2024a; Dudek et al., 2025b), high specific stiffness (Guo et al., 2022), high specific strength (Mahbod et al., 2020; Yan et al., 2024a; Yin et al., 2021), high energy absorption (Jiang et al., 2022; Hamzehei et al., 2023), optical applications (Jiménez et al., 2016; López Jiménez et al., 2016), negative stiffness adjustment (Tan et al., 2024c,b) and reusable shock mitigation (Yan et al., 2024b).

Lattice materials, a prominent class of mechanical metamaterials, are composed of periodically repeating unit cells with finely tuned three-dimensional geometries and distinctive connectivity, which collectively impart outstanding mechanical performance (Li et al., 2018; Liu et al., 2021; Li et al., 2021a). These lattices are classified as either bending-dominated or stretching-dominated, depending on their deformation mechanism (Deshpande et al., 2001a). At low relative densities, stretching-dominated lattices always exhibit high relative stiffness and strength that scale nearly linearly with relative density, whereas bending-dominated lattices provide more stable, nonlinear large-deformation behavior, with elastic modulus scaling quadratically with relative density (Deshpande et al., 2001b; Duan et al., 2020).

Although stretching-dominated lattices encompass a variety of geometric topologies, their compressive failure modes remain remarkably consistent (Duan et al., 2020; Zhang et al., 2023; Bonatti and Mohr, 2019b; Baishya et al., 2024). At low relative densities, elastic or plastic buckling of micro-components compromises overall deformation stability (Meza et al., 2014; Schaedler et al., 2011; Wang et al., 2021a). Take the octet truss lattices as an example: under compressive loading, axial forces in the struts dictate the deformation, while tensioned micro-rods restrain lateral expansion, thereby enhancing stiffness and strength (Deshpande et al., 2001b; Song et al., 2019). However, at low relative densities, the extreme slenderness of these micro-rods renders them susceptible to local instability, diminishing the load-bearing capacity of lattices. As strain continues to increase, this instability triggers a sudden load drop and ushers in an unstable deformation regime (Zhao et al., 2022; Kladovasilakis et al., 2022).

The primary strategy to address this is to redistribute internal stresses through optimized structural configuration, particularly in struts and nodes (Syrlybayev et al., 2024; Portela et al., 2018; Noronha et al., 2023). One of the earliest strategies to enhance nonlinear stability and boost energy absorption was to replace solid struts with hollow tubes, exploiting their higher moment of inertia (Wu et al., 2023; Queheillalt and Wadley, 2005b,a; Lan et al., 2025; Shu et al., 2025). By precisely tailoring hollow-rod cross-sectional geometry, the elastic buckling strength of stretching-dominated materials can be effectively tuned (Song et al., 2024). From an energy-absorption perspective, hollow truss lattices materials thus achieve significantly improved mechanical performance, surpassing that of solid truss lattices (Liu et al., 2024). Later, Bonatti et al. replaced the joints in octet hollow truss lattices with hollow spheres to reduce stress concentrations, further boosting strength and energy-absorption capacity and achieving stable performance under uniaxial compression at a relative density of 0.2 (Bonatti and Mohr, 2017). Similarly, Chen et al. introduced a new class of stretching-dominated mechanical metamaterials by optimizing body-centered cubic (BCC) truss lattices with hollow struts, nodal spheres, and smooth connections, enabling exceptionally high energy absorption at low densities (Chen et al., 2020) More recently, Zhang et al. embedded this hollow-strut concept within mesh-reinforced octet truss lattices, markedly boosting the effective bending stiffness of struts and delivering strong resistance to premature collapse, thereby securing nonlinear stability at a relative density of just 0.1 (Zhang et al., 2025, 2023). However, its stiffness and strength remain substantially lower than those of shell lattices. Additionally, Tancogne et al. demonstrated that octet truss lattices built with tapered, variable-section rods outperform those with equal-mass, constant-section rods in energy absorption: at a relative density of 0.2, the tapered-rod design delivers a notably more stable compressive response (Tancogne-Dejean et al., 2016).

Drawing on the smooth, non-intersecting, zero-mean-curvature geometry of triply periodic minimal surfaces (TPMS), researchers have developed a series of thin-shell lattice materials that mitigate stress concentrations at hollow-truss joints and enhance mechanical performance (Song et al., 2024; Han et al., 2015; Zhang et al., 2018; Jeong et al., 2024; Han and Che, 2018). Bonatti et al. extended this concept with a local bending-energy functional that minimizes maximum principal curvature, producing surfaces with superior smoothness that boost fatigue resistance and curb plastic localization (Bonatti and Mohr, 2019a). Using this approach, they designed cubic-symmetric smooth thin-shell metamaterials whose mechanical properties rival or exceed those of TPMS-like lattices. Compared to solid or hollow truss lattices, these shell-based lattices deliver higher average elastic modulus, greater yield strength, and improved energy-absorption efficiency (Bonatti and Mohr, 2019b).

While the above optimization strategy is effective at relative densities above 0.2, its scalability is limited at lower densities. At a relative density of 0.1, such lattices often exhibit persistent unstable oscillations in practical applications (Duan et al., 2020; Bonatti and Mohr, 2017; Tancogne-Dejean et al., 2019, 2018), or require compromising strength or stiffness to maintain stable nonlinear responses (Zhang et al., 2025, 2023). This raises a pressing question: can high elastic-plastic performance and robust nonlinear stability be simultaneously achieved at low relative densities?

In this work, we propose a feasible solution to address this challenge by integrating a stretching-dominated mechanism with a contact-enhanced mechanism, offering compensatory reinforcement to ensure stability under large deformations. To this end, we develop a new class of BCC shell lattices constructed with elliptical hollow struts and hollow spherical nodes, seamlessly connected through smooth transitions. These lattices are classified as completely smooth or incomplete smooth shell designs, both optimized to deliver an uncommon blend of high strength, stiffness, energy absorption, and stability at low relative densities. Their mechanical performance, examining geometric parameter effects, loading-direction dependence, and benchmarks against conventional BCC truss lattices, is assessed via numerical simulations and validated by compression tests. At a relative density of 0.1, the incomplete

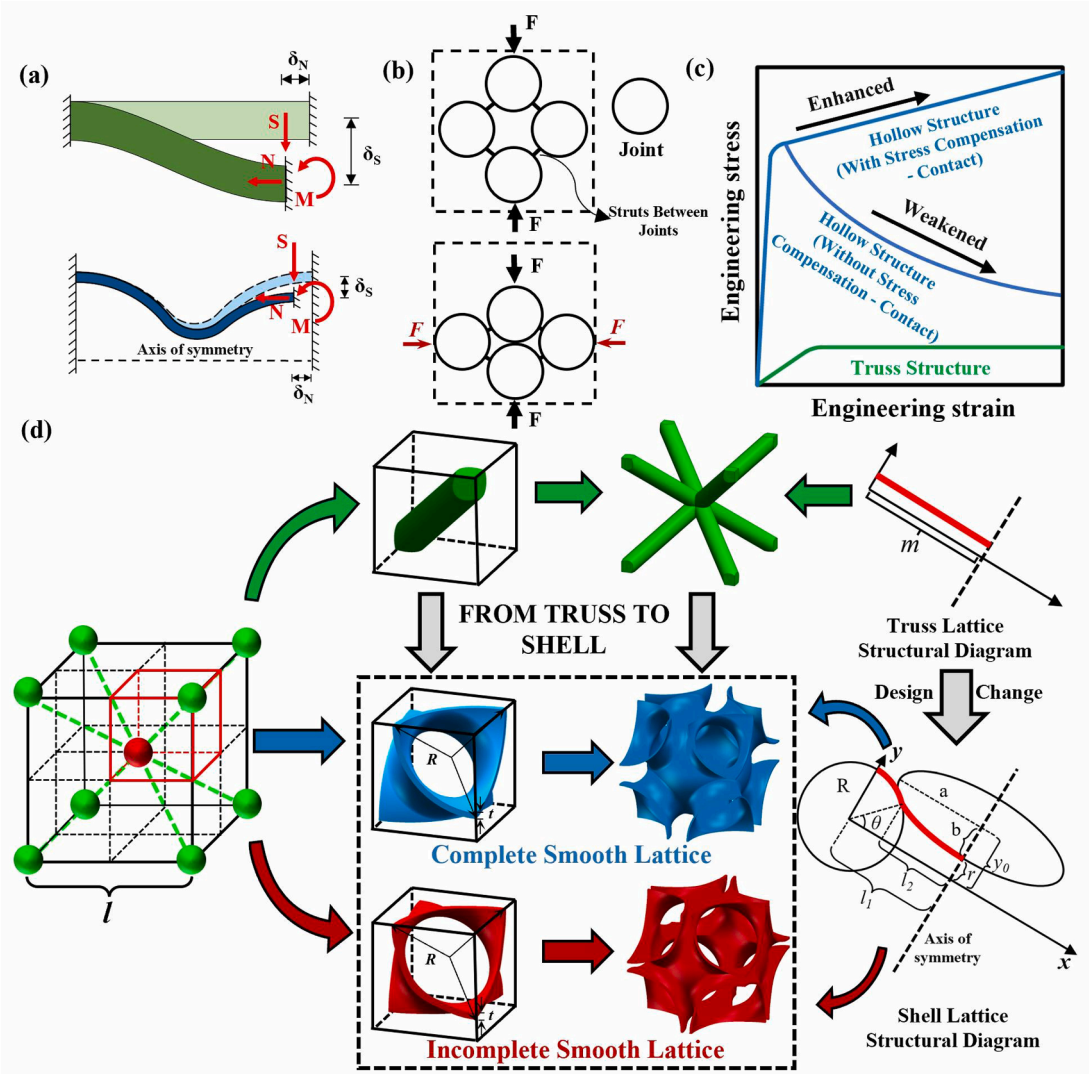

Fig. 1. (a) Simplified fixed-beam model at both ends of the truss structure and variable cross-section model of the hollow structure, showing deformations under axial compression, bending moment, and shear load. (b) The contact behavior arises from the controlled configuration of nodes and struts under applied loads. (c) By harnessing the improved mechanical response after node contact, the design mitigates performance loss due to instability at low relative densities, ensuring stable stress behavior throughout the nonlinear regime. (d) A general process for implementing the above mechanism on a BCC truss lattice to produce a novel shell lattice design. By introducing elliptical curves to mediate the transitional curvature between hollow sphere joints, the restructured system enables the design of two distinct lattice typologies: CSL and ISL.

smooth variants demonstrate superior specific stiffness, strength, and energy absorption, along with markedly more stable stress-strain responses compared to TPMS-like shell lattices.

2. Metamaterials

2.1. Shell lattices design driven by contact mechanisms

The design concept arises from two key fundamentals: the substantial disparity in bending moment, shear force, and buckling resistance between solid and hollow struts (Fig. 1a), and the stress-enhancement mechanisms triggered by contact interactions within the structure (Fig. 1b,c).To illustrate the proposed deformation mechanism, a simplified double-clamped beam model is presented in Fig. 1a.Under identical loading, hollow struts, particularly those with variable cross-sections, exhibit significantly smaller axial and shear deformations and achieve superior load-bearing capacity compared to their solid counterparts, owing to a larger moment of inertia. To address weak connections between struts and enable contact-induced stress-enhancement, high-stiffness nodal configurations are introduced, resulting in the 2D simplified model shown in Fig. 1b. When nodes come into contact during compression,

either between adjacent nodes or as local deformations reach the unit-cell boundary, they provide supplemental support. Integrating this intentionally engineered contact mechanism with low relative density, stretching-dominated configurations introduces an additional stress-compensation effect. When active, it enables continued stress enhancement even beyond the initial peak strength. In its absence, particularly at low relative densities, a weakening phenomenon may occur (Fig. 1c).

The mechanism is extended from the 2D to the 3D case and applied to the BCC truss lattices, leading to the following procedure for generating a class of shell lattices. Fig. 1c shows the cubic unit cell of a BCC lattice, with nodes highlighted in green and red to illustrate the design scheme. Each unit cell features two node types: eight one eighth nodes at corners of the cube, each shared by eight adjacent cells, and a single full node at its center. These nodes are linked by a solid green line. When the generatrix curve, rotated about this green axis, is straight, the result is a solid truss lattice. By redefining the generatrix curve and reconstructing the parametric modeling framework, a diverse array of shell lattices can be generated. To enhance internal support and activate a contact mechanism under large deformations, this design strategy prioritizes the nodal configuration, utilizing hollow spheres as the nodal elements. To achieve a smooth shell geometry reminiscent of TPMS lattices, thereby avoiding stress concentrations and improving resistance to bending and buckling, each hollow sphere is connected by hollow struts whose generatrix follows an elliptical curve, ensuring tangent continuity at the sphere-strut interfaces. When assembling a unit cell, the portion of the rotated shell strut shared with an adjacent cell must be removed, which may introduce surface discontinuities. Based on whether the lattices surface retains full geometric continuity, two distinct types are defined: the Complete Smooth shell Lattice (CSL) and the Incomplete Smooth shell Lattice (ISL). The generatrix curves governing the rotational construction are highlighted in red, while the parametric design is schematically illustrated in Fig. 1c. The following sections systematically dissect the parametric implementation framework, elucidating this geometry-driven transformation methodology.

2.2. Geometrical description of the shell lattices

Fig. 1c schematically illustrates the primary geometric parameters defining the proposed shell-lattice unit cell: l_1, l_2, R, r, a, b, t, θ, y_0. Here, l_1 is defined as half the distance between the red node and the green node, with a value of $\sqrt{3}l/4$, where l is the edge length of the cubic unit cell; l_2 represents the distance from the tangent point, where the elliptical curve meets the hollow-sphere joints, to the central axis indicated by the dashed line. R specifies the radius of the hollow sphere, while r denotes the vertical offset between the lowest point of the elliptical curve and the central axis.The parameters a and b denote the major and minor axes of the elliptical curve, respectively, and t specifies the thickness of shell. θ denotes the angle between the rotation axis and the line from the center of the hollow sphere to the contact point. y_0 denotes the offset distance from the elliptical center to the rotation axis.

Note that these geometric parameters are interdependent. To ensure smooth shell lattices, a set of internal equations describes the geometric relationships (rotational symmetry), positional constraints (nodal positions), elliptical configuration (major/minor axis ratio), and tangent continuity at the hollow sphere/elliptical curve interfaces, while enforcing identical tangent slopes at every connection point, as follows:

$$\begin{cases} R\cos\theta = l_1 - l_2 \\ y_0 - b = r \\ \frac{l_2^2}{a^2} + \frac{(R\sin\theta - y_0)^2}{b^2} = 1 \\ \frac{b^2}{a^2}\frac{l_2}{R\sin\theta - y_0} = -\cot\theta \end{cases} \tag{1}$$

Given a fixed length l_1, the remaining unknown parameters to be determined are R, r, θ, l_2, y_0, a and b. To reduce the number of variables, three key geometric control parameters (α, β, γ) are introduced.

$$\begin{cases} \alpha = r/R \\ \beta = l_2/l_1 \\ \gamma = a/b \end{cases} \tag{2}$$

Substituting Eqs. (2) into Eq. (1) yields:

$$\begin{cases} R\cos\theta = (1-\beta)l_1 \\ y_0 - \frac{a}{\gamma} = \alpha R \\ \frac{\beta^2 l_1^2}{a^2} + \frac{(\gamma^2 R\sin\theta - y_0)^2}{a^2} = 1 \\ \frac{\beta l_1}{R\sin\theta - y_0} = -\gamma^2\cot\theta \end{cases} \tag{3}$$

With four unknowns (R, θ, y_0, a) and three predefined control parameters (α, β, γ), the four independent simultaneous equations theoretically yield a unique solution. Through derivation (see Note.S1), these equations reduce to a θ-dependent implicit function:

$$\frac{\beta^2}{\gamma^2}\left(1 + \frac{\tan^2\theta}{\gamma^2}\right) = \left[\left(1 - \beta + \frac{\beta}{\gamma^2}\right)\tan\theta - \alpha(1-\beta)\sqrt{1+\tan^2\theta}\right]^2 \tag{4}$$

Solving the implicit equation yields θ as a function of the three predefined control parameters (α, β, γ), after which the remaining unknowns can be calculated as follows:

$$\begin{cases} R = \frac{(1-\beta))l_1}{\cos\theta} \\ y_0 = (1-\beta+\frac{\beta}{\gamma^2})l_1\tan\theta \\ a = l_1\gamma[(1-\beta+\frac{\beta}{\gamma^2})\tan\theta - \frac{\alpha(1-\beta)}{\cos\theta}] \end{cases} \tag{5}$$

Importantly, the CSL configuration forms only when $\tan < 1/\sqrt{2}$; otherwise, the ISL configuration emerges. Therefore, by modulating the parameters α, β, γ and t/l, a variety of structural configurations with diverse relative densities can be achieved. The relative density $\bar{\rho}$ is defined by the ratio of volume of the shell structure, directly obtained from 3D software, to the total volume of the unit cell as follow:

$$\bar{\rho} = \frac{V_S}{V_{tot}} \tag{6}$$

Where V_S represents the volume of the solid material within a single unit cell; and V_{tot} represents the bounding volume of the unit cell (the total volume of the unit cell itself).

To systematically explore the design space, we vary the three geometric control parameters at a fixed relative density (e.g., 0.1), which correspondingly adjusts the thickness-to-length ratio (t/l), thereby generating distinct lattices geometries for comparative analysis. For streamlined characterization, each configuration is represented by the parameter triad $<\alpha,\beta,\gamma>$, with representative examples shown in Figure S1. Parameters α and β have a pronounced effect on the hollow-sphere radius R and the thickness of the inter-nodal connecting shells t. For example, increasing α from 0.3 to 0.6 enlarges R by roughly 10%. In contrast, γ predominantly fine-tunes the structural details of the ISL and CSL configurations.

3. Numerical simulations

To comprehensively investigate the mechanical behavior of shell lattices across a broad spectrum of relative densities $\bar{\rho} \in \{0.01; 0.02; 0.05; 0.1; 0.2; 0.3; 0.5\}$ and geometrical ratios, $\alpha \in [0.05, 0.65]$, $\beta \in [0.05, 0.3]$, and $\gamma \in \{0.5; 1; 1.5; 2; 3\}$, both linear and nonlinear finite element analyses were conducted using the commercial software Abaqus.For comparison and validation, the same procedure was applied to the corresponding BCC truss lattice metamaterial.

3.1. Basis material

An isotropic elasto-plastic model with isotropic hardening behavior is employed to characterize the mechanical properties of the base material. This model choice aligns with extensively validated methodologies in the field (Zhang et al., 2025; Li et al., 2025; Zhao et al., 2025; Meyer et al., 2024). For 316L stainless steel, the average elastic modulus is approximately 180 GPa, the Poisson's ratio is 0.3, and the density is 7.3 g/cm^3. The yield strength, defined at a 0.2% offset, is approximately 450 MPa. The ultimate tensile strength is 760 MPa, corresponding to a true tensile strain of 0.2. The true stress-strain curve shown in Figure S2, along with the corresponding mechanical properties (yield strength, ultimate strength, and ultimate strain), was obtained from tensile tests on dog-bone specimens, offering detailed insights into the mechanical behavior of the basis material.

3.2. Unit-cell simulation

Unit cell models with periodic boundary conditions are employed to predict elastic-plastic behavior under small deformations.The shell meshing process begins by generating representative elementary geometries, which are thickened along their inward surface normal to achieve the target relative density. This approach maintains the smooth outer surface required by the CSL design and avoids the geometric interference between neighboring spherical nodes that bidirectional thickening would introduce at higher densities. The elementary structure is then replicated, mirrored, and translated to form a periodic shell mesh that fills the unit cell. For relative densities of 0.01 and 0.02, shell lattices were meshed with at least 74,000 tetrahedral elements (C3D10 type) to ensure computational accuracy. All truss lattices, as well as shell lattices with relative densities of 0.05 or higher, are discretized using first-order solid elements (C3D8R type), with a minimum of five elements along the radial direction and four elements through the thickness, respectively. To further ensure accuracy, meshes consisting of approximately 84,000 elements were used for the shell lattices and 62,000 elements for the truss lattices. As relative density increases, mesh refinement with higher element density is applied to improve the accuracy of stress and strain field predictions. Details of the mesh configurations are provided in Figure S3. Periodic boundary condition is implemented for the cell model, with linear constraint equations established between parallel boundary surfaces to enforce displacement compatibility at the corresponding boundary discrete nodes (Li and Wongsto, 2004). Elastic moduli, Poisson's ratio, and Zener's ratio were extracted from uniaxial compression simulations along the principal directions and pure shear simulations. The applied strain magnitude was limited to $1 \times 10^{-4}$to ensure a linear elastic response. The yield strength was determined using the 0.2% plastic strain offset criterion, defined as the maximum axial stress at which the accumulated residual plastic strain reaches this threshold.

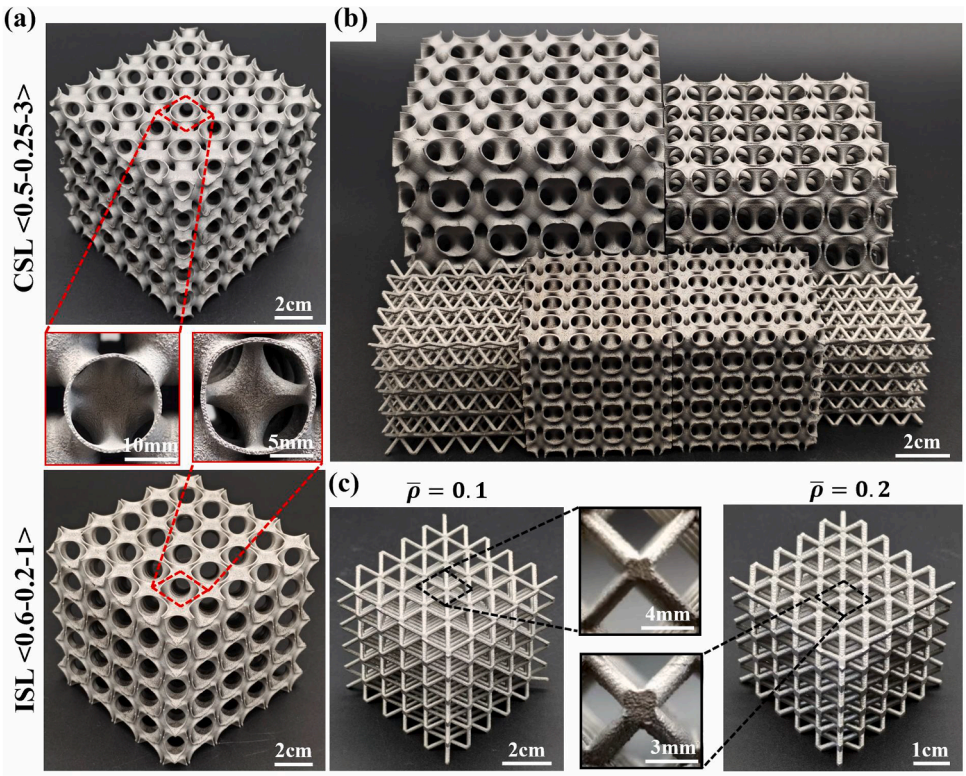

Fig. 2. (a) Isotropic views of the shell lattice samples CSL <0.5,0.25,3> and ISL <0.6,0.2,1>, along with zoomed-in details of their spherical nodal structures. (b) Views of untested shell and truss lattice samples of relative densities of about 0.1 and 0.2. (c) Photographs of the BCC truss lattice samples, along with partially magnified views.

3.3. Large deformation compression simulation

To further investigate the large-deformation mechanical behavior of lattice materials, cubic symmetric configurations composed of 3×3×3 unit cells were generated, containing at least 3 million solid elements to ensure computational accuracy. The element type used is identical to that employed in the unit cell model. The lattice models were sandwiched between two rigid platens, and large-deformation contact simulations were performed using an explicit dynamic integration algorithm. A self-contact boundary condition was applied with a friction coefficient of 0.2, a value commonly adopted and physically reasonable for self-contact between stainless steel surfaces (Bonatti and Mohr, 2019a; Tancogne-Dejean et al., 2018). During compression, the base platen remains fully constrained, while the top platen undergoes quasi-static, displacement-controlled loading until 50% densification is achieved, with the kinetic-to-internal energy ratio maintained below 1%.

4. Experiment

The experimental framework is designed to acquire mechanical data for the base material used in numerical simulations, thereby facilitating validation of the computational model.

4.1. Sample preparation

Configurations CSL and ISL were chosen from the shell-lattice family and experimentally compared against a conventional bending-dominated BCC truss lattice to assess their mechanical performance (Fig. 2). The shells selected for fabrication exhibited the highest uniaxial compressive yield strength at each relative density: for $\bar{\rho} = 0.1$, CSL <0.5,0.25,3> and ISL <0.6,0.2,1>; for $\bar{\rho} = 0.2$, CSL <0.5,0.2,2> and ISL <0.5,0.3,1>. All specimens were fabricated using selective laser melting technology, employing stainless steel 316L powder (Concept Laser GmbH) with a controlled particle size distribution of 20–50 μm. For specific details regarding the printing equipment, please refer to Table S1. To ensure high printing quality, the laser power and scanning speed were carefully set to 200 W and 8 m/s, respectively. Post-processing involved a 20-minute ultrasonic bath to remove residual 316L powder particles, thereby preserving surface integrity.

Fig. 2 presents representative specimens alongside zoomed-in details that highlight the printing features. For each configuration, a 5×5×5 unit cell arrangement was evaluated at relative densities of 0.1 and 0.2. Two replicates per configuration were fabricated to

Table 1
Measured dimensions and mass of the printed samples.

Type	Direction 1 (mm)	Direction 2 (mm)	Direction 3 (mm)	Mass (g)	Relative density (%)
BCC Truss	49.94	49.98	50.07	90.63	9.55
	49.98	49.89	49.93	90.12	9.52
	39.91	40.11	39.82	92.79	19.16
	40.03	40.00	40.04	92.30	18.99
CSL	97.12	97.62	96.92	726.72	10.14
<0.5,0.25,3>	97.30	97.22	96.93	722.13	10.09
CSL	52.60	52.26	52.31	228.60	20.38
<0.5,0.2,2>	52.92	52.33	52.60	232.61	20.47
ISL	82.58	83.40	83.00	454.82	10.19
<0.6,0.2,1>	83.20	83.40	82.60	449.27	10.18
ISL	52.64	52.53	52.48	230.50	20.36
<0.5,0.3,1>	52.53	52.08	52.43	230.12	20.57

minimize stochastic variation and improve statistical reliability. Detailed geometric dimensions are listed in Table 1 with maximum dimensional deviations between the as-designed and as-built specimens kept below 0.3 %.

4.2. Uniaxial tensile test on dog bone specimens

To determine the mechanical properties of the base material (316L stainless steel), three dog-bone tensile specimens were fabricated following ASTM E8/E8M standards, using the same laser processing method applied to the lattice specimens. Uniaxial tensile tests were carried out on the printed specimens using a 50 kN universal testing machine (Instron 5569) at a nominal strain rate of $10^{-3}s^{-1}$. Axial tensile forces were directly recorded from the testing machine, while axial tensile displacement was calibrated using a mechanical clamping extensometer.

4.3. Uniaxial compression testing of lattice materials

For the lattice samples, the compressive mechanical response was characterized using a CSS-WAW600 universal testing machine equipped with a 500 kN load cell, under a quasi-static strain rate of $10^{-3}s^{-1}$. Prior to testing, the specimens were placed between two steel plates with controlled preloading to prevent slippage, as illustrated in Figure S4. To mitigate inherent mechanical measurement errors of the tester, front-view videos of the samples were captured to monitor lateral-face deformations and, using an in-house digital image correlation algorithm (Eberl et al., 2006), correct the load and displacement curves. Following the methodology of Bonatti and Mohr (2017), Young's modulus was calculated from the average local axial strain measured in the central row of unit cells. Engineering stress and strain were then obtained by dividing the measured force and the calibrated global displacement by the cross-sectional area and height of samples, respectively.

5. Results and discussion

This section covers three main topics: (1) the anisotropic mechanical properties of CSL, ISL, and BCC truss lattices; (2) the influence of CSL and ISL design parameters on elastic modulus and yield strength; and (3) the large-deformation behavior of CSL and ISL, including stress-strain responses and structural features arising from our design method.

The sets <0.6,0.2,1> (ISL) and <0.5,0.25,3> (CSL) yield the highest strengths at a relative density of 0.1 and exhibit directional dependence characteristic of optimal configurations across densities. Focusing on low-density performance, all subsequent simulations use these parameter sets to clearly illustrate the evolution of mechanical behavior and anisotropy over the full range of relative densities.

5.1. Elastic behavior

For shell and truss lattices exhibiting cubic symmetry, an anisotropy evaluation framework is required to quantitatively assess the effect of loading orientation on the elastic response. The Zener ratio, a widely used metric for elastic anisotropy in cubic crystal systems, is defined as follows (Chen et al., 2024):

$$Z = \frac{2(1+\mu)G}{E} \tag{7}$$

Where E, G and μ denote the elastic modulus, shear modulus, and Poisson's ratio of the cubic lattices in the principal direction, respectively. Elastic isotropy in cubic crystals occurs only when the Zener ratio equals 1, enforcing the requisite proportional relationships among these three moduli. Any deviation from unity signifies direction-dependent elastic behavior.

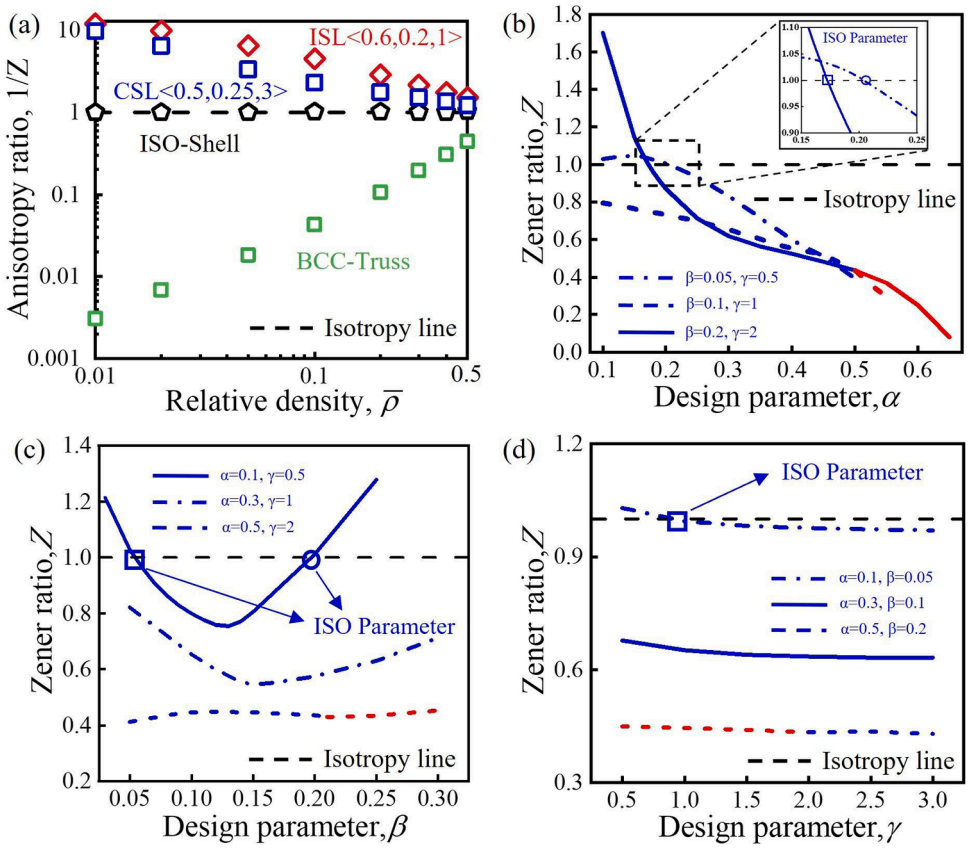

Fig. 3. Elastic anisotropy and isotropy of shell and truss lattices. (a) Evolution of the Zener ratio versus relative density for truss lattices and for the CSL $< 0.5, 0.2, 2 >$, ISL $< 0.6, 0.2, 1 >$ and ISO-shell. (b-d) Influence of geometric parameters α, β and γ on the Zener anisotropy ratio at a relative density of 0.1.

Table 2
Geometric parameters of isotropic lattices at various relative densities.

Relative density		0.01	0.02	0.05	0.10	0.20	0.30	0.40	0.50
Parameter	α	0.192	0.185	0.333	0.19	0.189	0.315	0.425	0.46
	β	0.20	0.20	0.05	0.05	0.20	0.25	0.30	0.25
	γ	2	2	1	1	1.5	2	2	3

Fig. 3a plots the isotropy coefficient Z against relative density for BCC truss lattices and the two shell configurations (CSL and ISL). A black dashed line at $Z = 1$ denotes perfect elastic isotropy. ISL and CSL results are shown in red and blue, respectively, while black markers highlight parameter sets that achieve structural isotropy at each density. Notably, elastic isotropy is achieved across all considered relative densities. Table 2 ists the corresponding structural parameters for each density. For BCC truss lattices, the anisotropy coefficient falls from 328 at a relative density of 0.01 to 2.27 at 0.5. Shell lattices follow an opposite pattern: anisotropy decreases with increasing density, from 0.0997 (CSL) and 0.0839 (ISL) at $\overline{\rho} = 0.01$ to 0.709 (CSL) and 0.663 (ISL) at $\overline{\rho} = 0.5$. Overall, the ISL $< 0.6, 0.2, 1 >$ configuration exhibits more pronounced anisotropy than CSL $< 0.5, 0.25, 3 >$.

Fig. 3(b-d), at a relative density of $\overline{\rho} = 0.1$, illustrate the anisotropy levels of various lattice configurations, demonstrating how the isotropy coefficient changes with structural parameters. In these plots, red lines denote ISL configurations, and blue lines denote CSL configurations. The Zener ratio decreases as α increases, but the anisotropy pattern varies by configuration. For example, $\beta = 0.2$ and $\gamma = 2$, anisotropy first declines then rises, reaching perfect isotropy at $\alpha = 0.22$. When α and γ are held constant, varying β alone can produce two distinct isotropic lattices. In CSL configurations, the Zener ratio falls and then rises with β. In contrast, changes in γ have minimal impact, causing only a slight drop in the Zener ratio as γ increases.

For cubic crystalline materials, the anisotropic Young's modulus can be expressed as (Meyers and Chawla, 2008):

$$\frac{1}{E_{ijk}} = \frac{1}{E} - \frac{Z-1}{2G}(l_{i1}^2 l_{j2}^2 + l_{j2}^2 l_{k3}^2 + l_{i1}^2 l_{k3}^2) \tag{8}$$

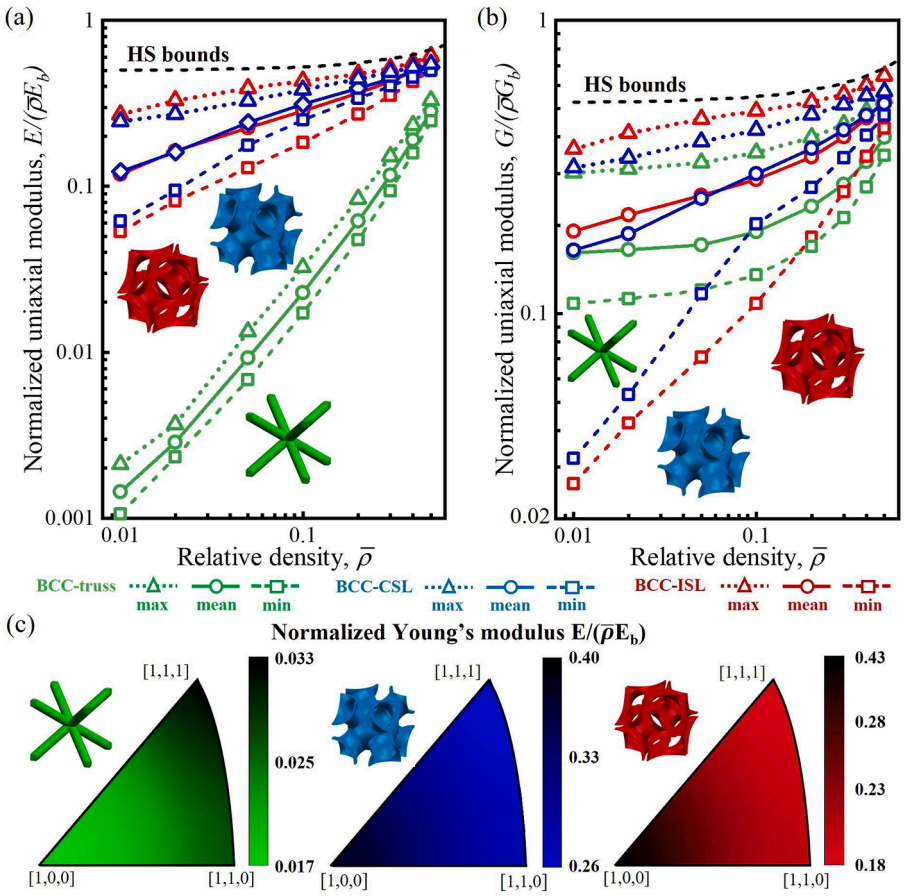

Fig. 4. A direct comparison of the maximum, minimum, and average elastic moduli between BCC truss lattices and the proposed CSL and ISL across varying relative densities: (a) Young's modulus and (b) shear modulus (dashed lines indicate the Hashin-Shtrikman bounds for an isotropic porous solid). (c) Polar plot showing the directional distribution of Young's modulus for BCC truss, CSL, and ISL shell lattices at $\overline{\rho} = 0.1$.

Where, E_{ijk} denotes the Young's modulus along the crystallographic direction $[ijk]$, and l_{i1}, l_{j2}, l_{k3} represent the direction cosines of the orientation vector relative to the principal crystal axes.

Fig. 4a shows the maximum, minimum, and average relative Young's moduli of three lattice types, evaluated over all directions, plotted against relative density. To ensure comparability, each modulus is normalized by the product of the base material modulus and the relative density, effectively mitigating differences in base material properties and clarifying overall trends. CSL and ISL exhibit their stiffest and softest Young's moduli along the [100] and [111] directions, respectively, while the opposite is true for truss lattices, as depicted in Fig. 4c and Figure S5. Both shell lattices exhibit superior specific stiffness across all loading directions within the relative density range of 0.01-0.5, consistently outperforming corresponding truss lattices and approaching the Hashin-Shtrikman (HS) bounds more rapidly. The Young's modulus of CSL in the [100] direction is lower than that of ISL, with the ratio (E_{CSL}/E_{ISL}) remaining around 90 % and showing no significant decrease as relative density increases. While the average Young's moduli of CSL and ISL are comparable, CSL displays weaker directional dependence under uniaxial compression. At a relative density of 0.1, the normalized stiffness of the CSL peaks at 0.39 and falls to 0.26, corresponding to approximately 12-fold and 15.3-fold increases, respectively, over the maximum and minimum values of the truss lattices. At a relative density of 0.5, the maximum and minimum values for the ISL attain respectively almost 91.2 % and 75.6 % of the HS bounds.

The directional dependence of shear modulus is determined as (Meyers and Chawla, 2008):

$$G_{ijk} = G(1 + 2(\frac{1}{Z} - 1)(a_{31}^2 a_{21}^2 + a_{32}^2 a_{22}^2 + a_{33}^2 a_{23}^2)) \tag{9}$$

Where, a_{ij} are the direction cosines representing the angle between the i axis of the transformed reference frame and the j axis of the material reference frame.

Fig. 4b shows how the maximum and minimum relative shear moduli of the three lattices evolve with relative density. Across all examined relative densities, the average shear moduli of CSL and ISL are comparable, both surpassing that of BCC truss lattices and progressively approaching the theoretical HS upper bound as density increases. Both shell lattices exhibit their minimum shear modulus on the {110} planes (shear direction [110]) and their maximum shear modulus along [100]. For BCC truss lattices, the

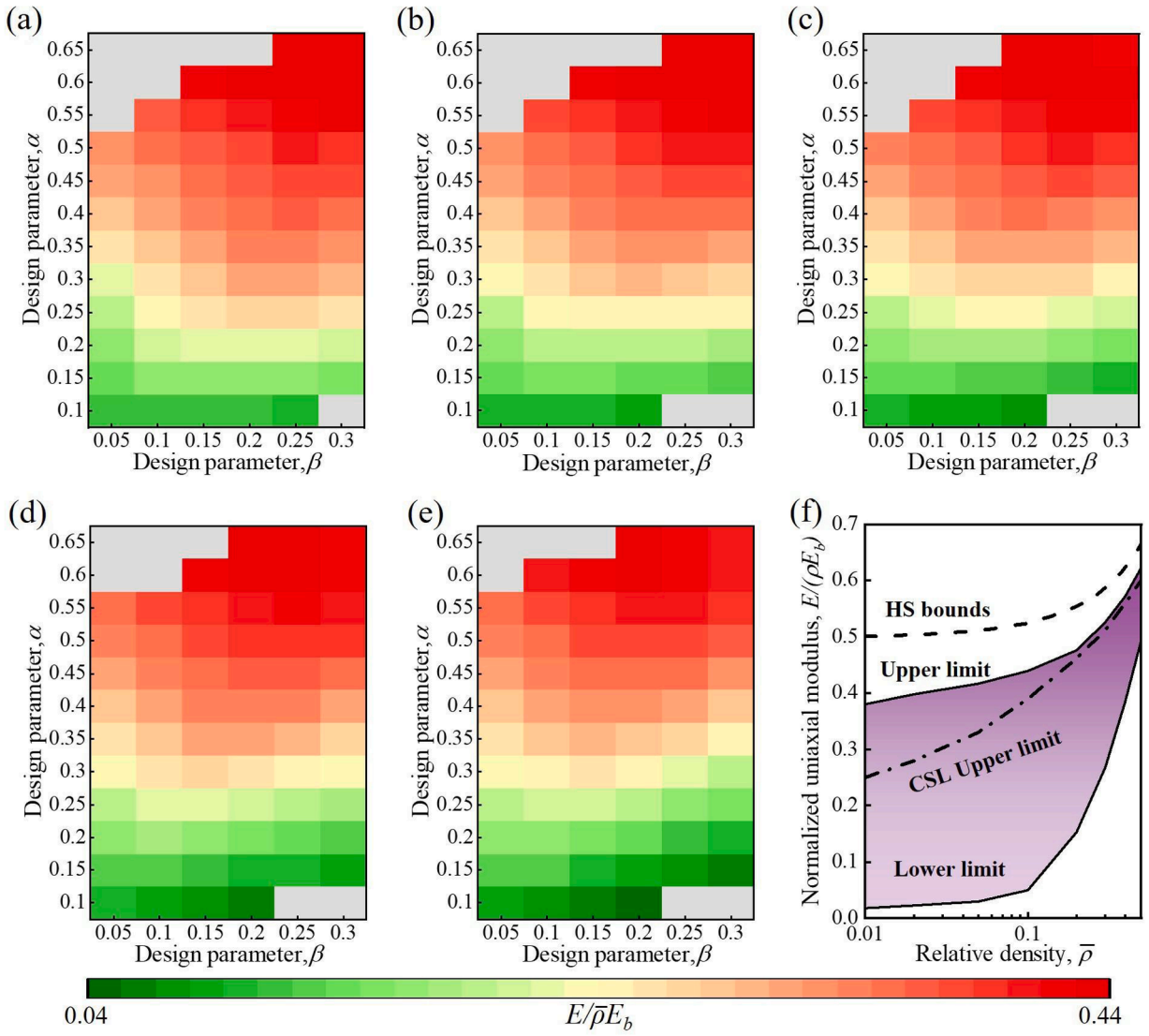

Fig. 5. (a-e) At a relative density of 0.1, the normalized elastic modulus is plotted as a function of parameters α and β with γ fixed at 0.5, 1.0, 1.5, 2.0, and 3.0, respectively. (f) Range of normalized elastic modulus as a function of relative density.

maximum also aligns with the {100} planes. The maximum shear modulus of both shell lattices always exceed that of the truss lattices, whereas their minimum shear modulus surpass the truss lattices only at relative densities above 0.1. At a relative density of 0.1, the normalized shear modulus of the CSL peaks at 0.423 and falls to 0.203, corresponding to approximately 1.2-fold and 1.5-fold increases, respectively, over the maximum and minimum values of the truss lattices. At a relative density of 0.5, the maximum and minimum values for the ISL attain respectively almost 91.2 % and 62.6 % of the HS bounds.

The multi-parameter design offers a wide range of lattice configurations. Using a relative density of 0.1 as an example, Fig. 5 and Fig. 6 illustrate the general trends in how varying design parameters influence the elastic and shear moduli along the principal direction.

Fig. 5(a-e) illustrates the influence of design parameters α and β on the normalized elastic modulus ($E/\overline{\rho}E_b$), with its distribution remaining nearly unchanged as γ increases. The normalized elastic modulus generally increases with α, peaking at approximately 0.44 near $\alpha = 0.6$ before slightly declining. In contrast, its variation with β is non-monotonic: the normalized modulus rises and then falls, and the β value at which Young's modulus is maximized shifts from 0.1 to roughly 0.25 as α increases. Although γ changes the shell lattice configuration and thus alters the exact modulus values, the overall distribution patterns remain similar.

Fig. 5(f) shows how the maximum and minimum elastic moduli vary with relative density, illustrating the range achievable with the BCC-based shell design scheme. Both the upper and lower bounds of the elastic modulus rise with relative density: ISL consistently defines the upper bound, CSL the lower, with upper bound of CSL highlighted in the plot. As relative density rises, upper bound of

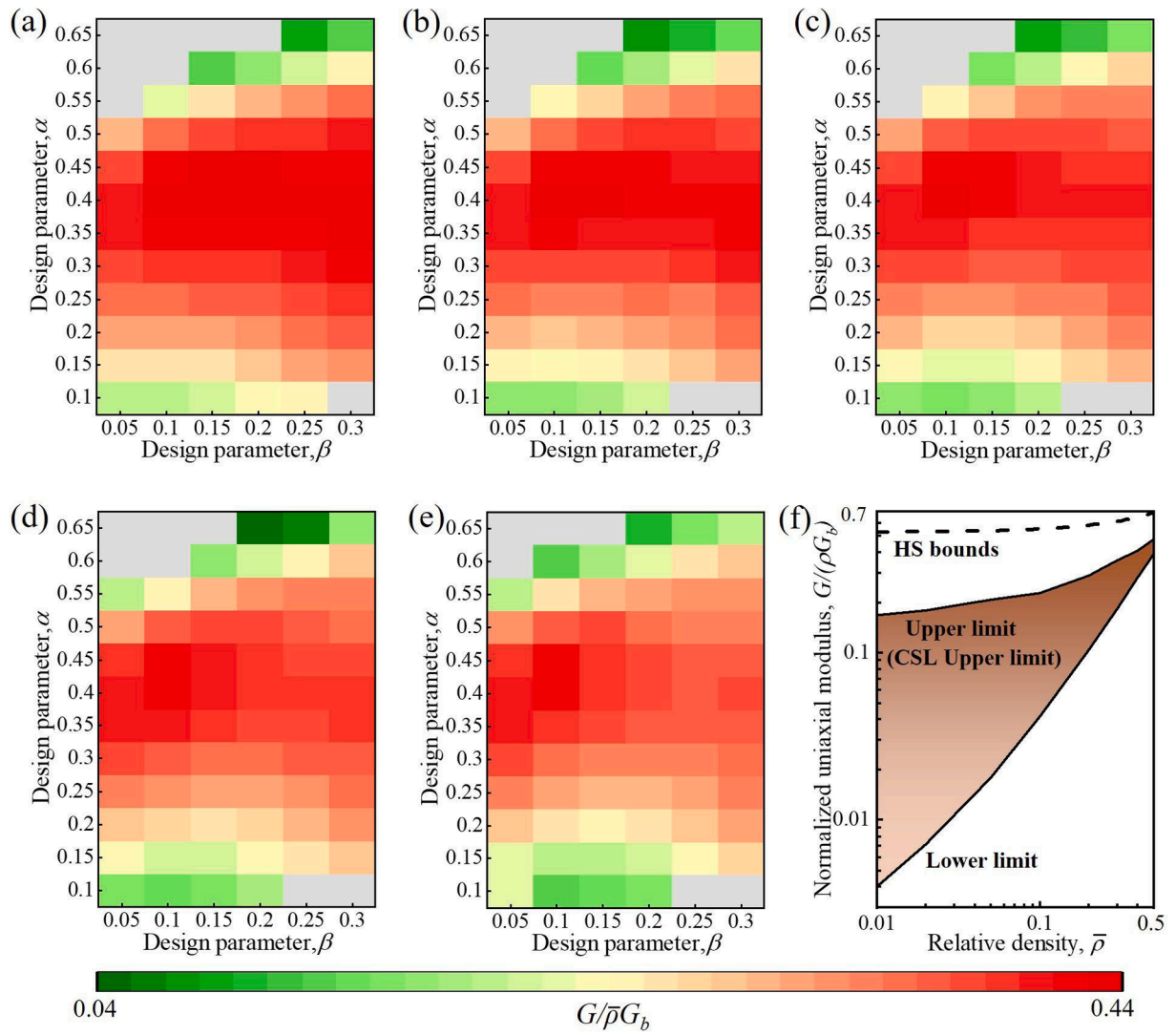

Fig. 6. (a-e) At a relative density of 0.1, the normalized shear modulus is shown as a function of parameters α and β with γ set to 0.5, 1.0, 1.5, 2.0, and 3.0, respectively. (f) Range of the normalized shear modulus attainable through shell design and its variation with relative density.

CSL converges toward that of ISL, with the ratio E_{CSL}/E_{ISL} increasing from 0.658 at $\overline{\rho} = 0.01$ to 0.965 at $\overline{\rho} = 0.5$, as both bounds progressively approach the HS bounds.

Fig. 6(a-e) illustrates the variation of normalized shear modulus with geometric parameters α, β and γ. The shear modulus initially increases with α, peaking in the range of $\alpha = 0.35 - 0.5$, and then gradually decreases as α continues to increase. At low α values (below 0.3), the shear modulus shows a decreasing-then-increasing trend with β, whereas at high α values (above 0.55), it increases monotonically with β. When α falls within the range of 0.35-0.5, the shear modulus shows minimal variation with β. Similar to the elastic modulus, the distribution pattern of the shear modulus shows limited sensitivity to variations in γ. Fig. 6(f) presents the upper and lower bounds of the shear modulus attainable under different parameter configurations, both increasing with relative density and gradually approaching the HS boundary. Notably, CSL achieves both the upper and lower bounds.

5.2. Yield strength

Fig. 7(a) illustrates the evolution of the normalized uniaxial yield strength as a function of relative density. Yield strength in CSL and ISL configurations peaks along the [100] direction and is lowest along the [111] direction, a trend reversed in their truss counterparts, as highlighted in 7(c). Clearly, both CSL and ISL outperform BCC lattices in terms of maximum, average, and minimum yield strength. Specially, at a relative density of 0.1, the normalized yield strength of the CSL peaks at about 0.5 and falls to 0.28, representing roughly 1.61-fold and 4-fold increases over the maximum and minimum values of the truss lattices, respectively. Fig. 7(b) displays the anisotropy of the yield strength. In general, yield strength anisotropy decreases with increasing relative density across all

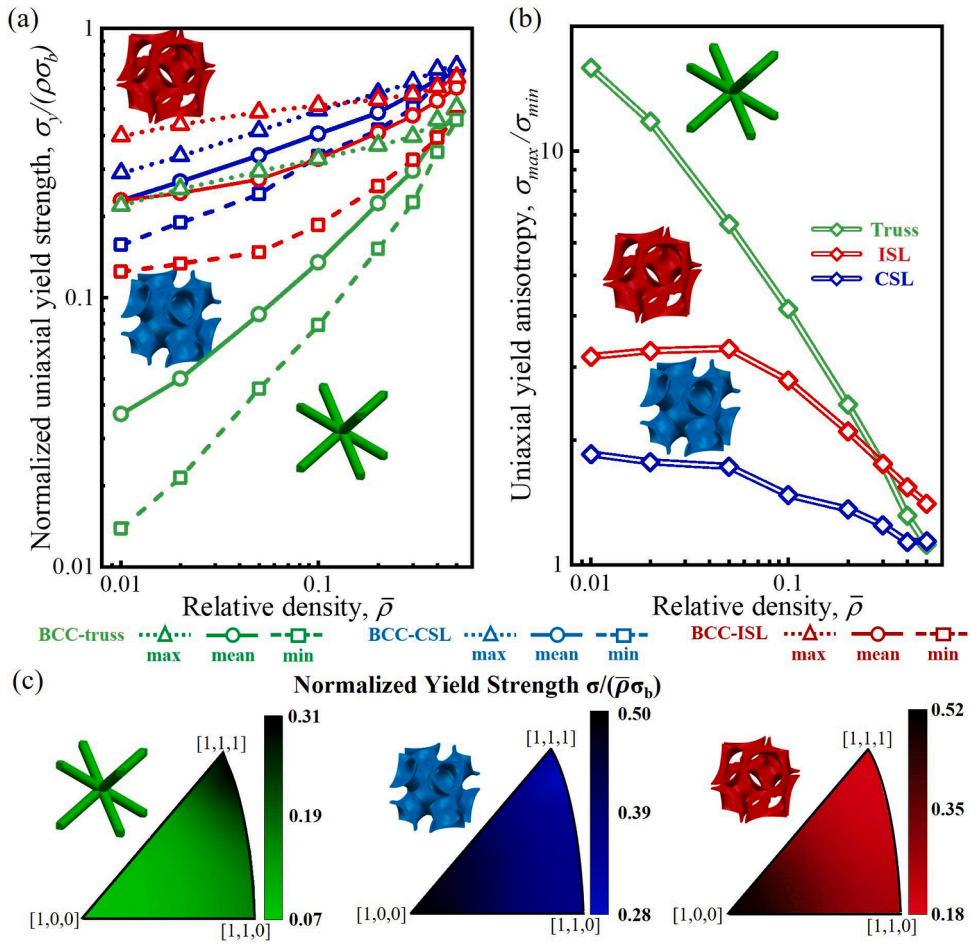

Fig. 7. (a) Comparison of yield strength between BCC truss lattices and the proposed CSL and ISL across various relative densities. (b) The ratio of maximum to minimum uniaxial yield strength across different loading directions as a function of relative density. (c) Polar plot of the directional distribution of yield strength for BCC truss lattices, CSL, and ISL shell lattices at a relative density of 0.1.

configurations. CSL consistently exhibits lower yield anisotropy than the truss lattices, whereas ISL shows reduced anisotropy only at relative densities below 0.3. At a relative density of 0.01, the maximum-to-minimum yield strength ratio reaches 15.85, which is nearly 10 times that of the CSL.

Fig. 8(a-e) quantifies achievable bounds and parameter sensitivity for the yield strength of CSL and ISL under [100] loading. The observed yield strength trend correlates strongly with that of the normalized elastic modulus in this direction. The normalized yield strength increases with α, peaking at about 0.52 in the range of $\alpha = 0.55 - 0.65$. With α and γ fixed, yield strength first increases and then decreases with β. The inclusion of β introduces additional design complexity, leading to a slight reduction in yield strength as β increases. Fig. 8(f) shows the upper and lower bounds of yield strength attainable under various parameter configurations. Notably, ISL exhibits the global upper bound, and the upper bound of CSL is also included for comparison. These upper bounds converge progressively with increasing relative density, reaching near equivalence beyond $\bar{\rho} = 0.3$. This convergence is quantified by the ratio $\sigma_{CSL}/\sigma_{ISL}$ which rises from 0.699 at $\bar{\rho} = 0.01$ to 0.989 at $\bar{\rho} = 0.5$.

Fig. 9 demonstrates normalization of elastic modulus and yield strength against relative density using the Gibson-Ashby law, providing a basis to quantify performance differences between tube and shell lattice configurations. CSL and ISL configurations demonstrate significant synergistic enhancement in both properties across all densities. Both outperform benchmark shell and hollow truss lattices in normalized Young's modulus and yield strength, with the stiffness of ISL advantage increasing markedly at lower relative densities. At a relative density of 0.01, ISL has a normalized Young's modulus of 0.38, which is 7.6 times that of the BCC hollow truss lattices and 25.6 times that of the BCC solid truss lattices. CSL registers 0.245 under identical normalization. Below $\bar{\rho} = 0.2$, ISL demonstrates substantial stiffness advantages over conventional shell lattices. Beyond this threshold, the normalized Young's moduli of ISL, CSL, and shell lattices converge to near-equivalence. Regarding normalized yield strength, CSL and ISL lattices show pronounced advantages, consistently outperforming other tube and shell configurations across all relative densities. At a relative density of 0.1, the normalized yield strength of ISL reaches 0.517 versus 0.495 for CSL. This represents a 1.38-fold increase over smooth-surface BCC shell lattices, 3.04-fold over BCC tube lattices, and 4.7-fold over solid BCC truss lattices. Collectively, the proposed CSL and ISL

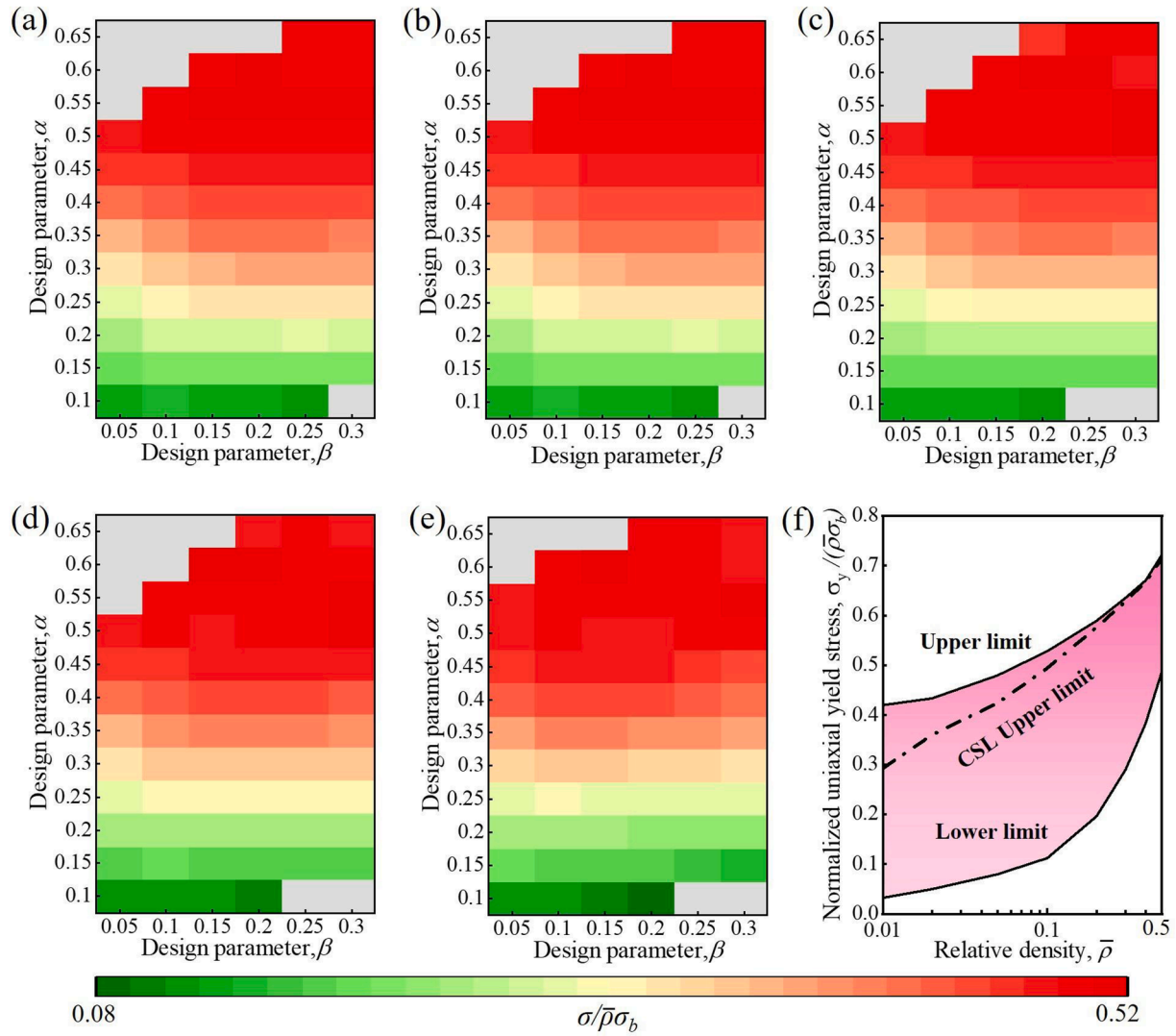

Fig. 8. Evolution of normalized yield strength as a function of parameters α, β, and γ with γ set to 0.5, 1.0, 1.5, 2.0, and 3.0 in panels (a) through (e), respectively. (f) Variation of normalized yield strength, including upper and lower bounds, as a function of relative density.

lattices deliver exceptional normalized stiffness alongside superior compressive strength across both low and high relative densities, outperforming existing tube and shell designs.

5.3. Large deformation compression response

Fig. 10 shows the compression responses of BCC truss lattices, CSL, and ISL–obtained via finite-element simulations at relative densities of 0.01, 0.05, 0.10, 0.20, 0.30 and 0.50. All architectures exhibit linear elasticity obeying Hooke's law initially. Beyond this regime, distinctive nonlinear behavior emerges during large-strain compression, where mechanical responses correlate strongly with both parametric design and relative density.

For both shell lattices at relative densities of 0.01 and 0.05, the compressive response features an initial linear regime. Beyond this, stress rapidly peaks at 1.4 MPa ($\varepsilon = 0.005$) and 11.34 MPa ($\varepsilon = 0.044$), followed by oscillations. At the lower density, however, the initial peak stress falls markedly below the predicted yield strength. This discrepancy arises because elastic buckling or local shell buckling deformations occur prior to plastic yielding. This buckling behavior is visualized in Fig. 11, which compares deformation modes of BCC truss lattices, CSL, and ISL. Analysis of Fig. 10 (stress-strain) and Fig. 11 confirms severe localized plastic deformation in CSL and ISL at $\bar{\rho} = 0.05$, inducing structural buckling. Consequently, significant stress oscillations emerge at low relative densities. Crucially, the spatial correlation between high-strain deformation zones and stress reduction regions directly demonstrates how buckling compromises structural integrity under low-density conditions. This severe localized deformation also leads to pronounced strain localization clusters in both shell lattices, particularly in ISL. Despite these deformation characteristics, CSL and ISL exhibit

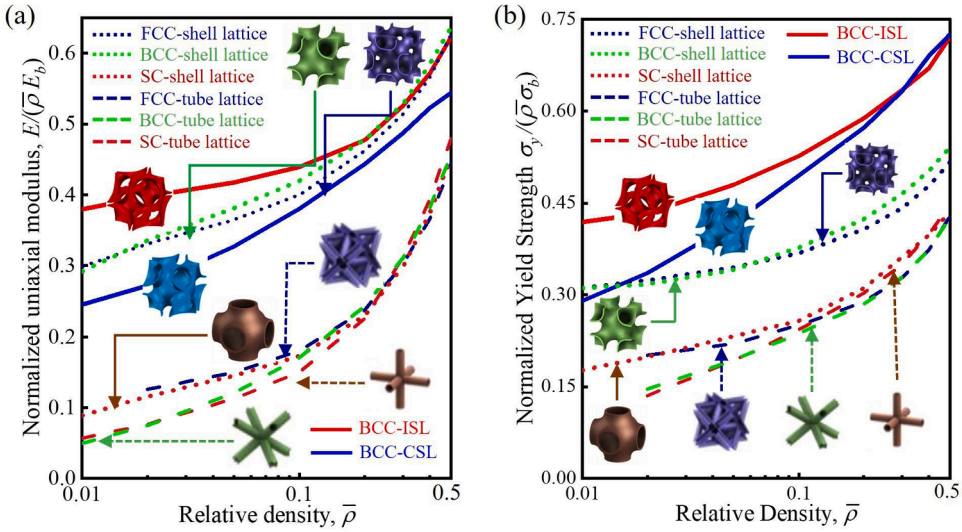

Fig. 9. Comparative mechanical property-density relationships: Normalized (a) Young's modulus and (b) yield strength for shell lattices (CSL, ISL), tube lattices, and benchmark topologies (Bonatti and Mohr, 2019b; Tancogne-Dejean and Mohr, 2018).

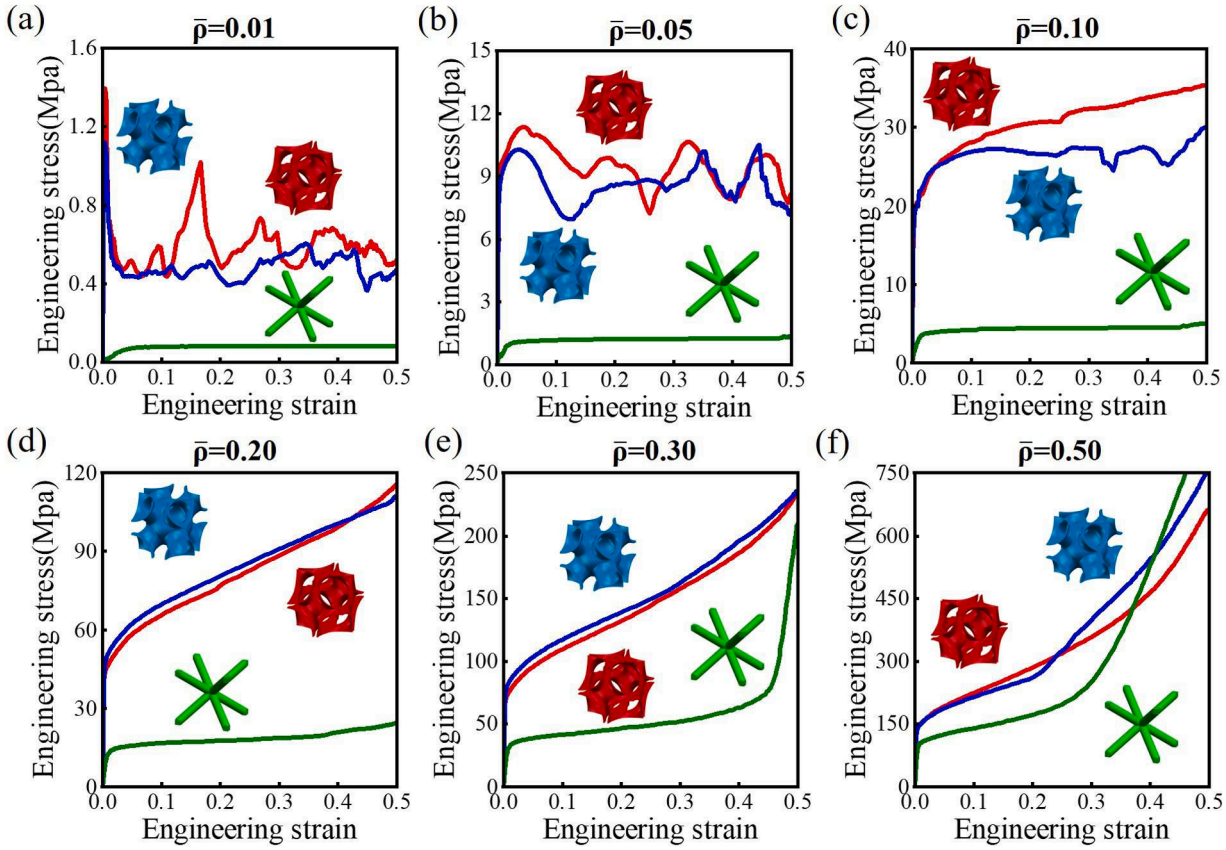

Fig. 10. Engineering stress-strain curves under quasi-static compression (50% strain limit) for CSL, ISL and BCC truss lattices at $\overline{\rho}=0.01$, 0.05, 0.10, 0.20, 0.30 and 0.50.

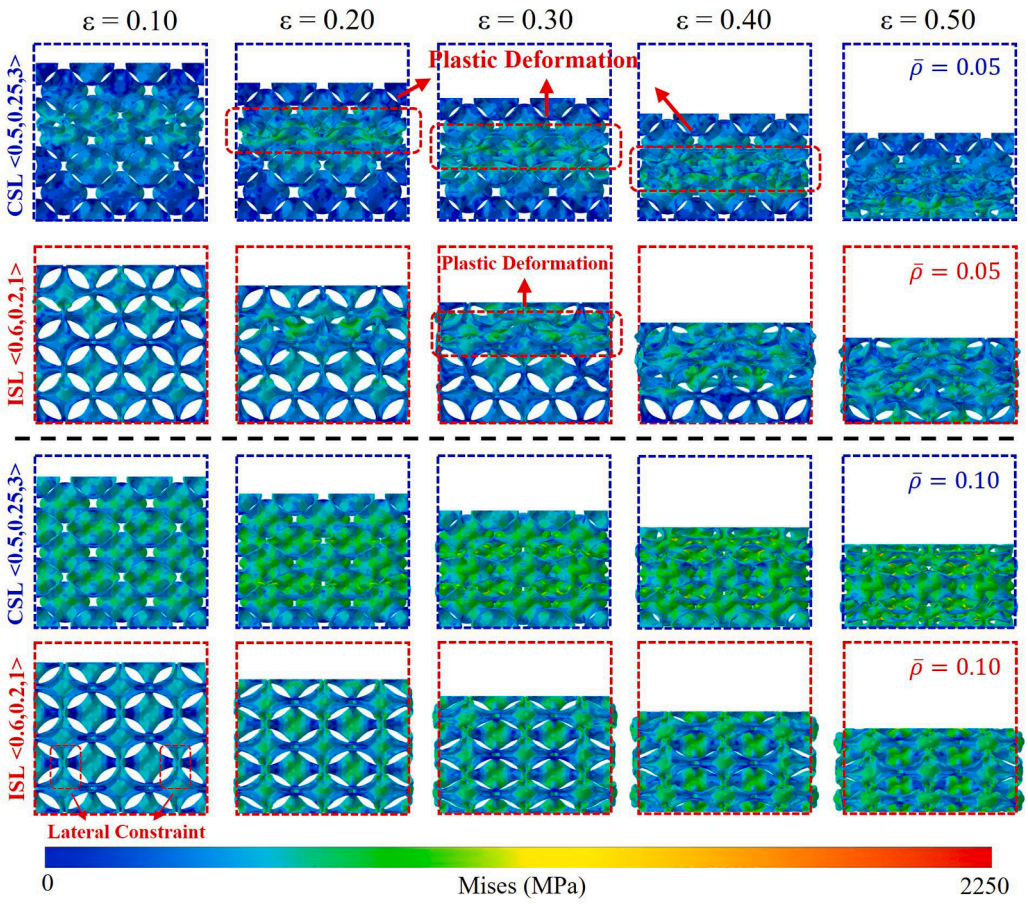

Fig. 11. Stress distribution diagrams of CSL and ISL lattices under deformation.

significantly higher yield strength and nonlinear phase strength than BCC truss lattices, and a more stable nonlinear response than certain lattices expressly engineered for nonlinear stability - a key advantage stemming from their shell-based design (see Figure S8). While BCC truss lattices maintain consistent stress stability across all nonlinear phases and densities (attributable to their bending-dominated mechanism), their overall strength remains consistently lower.

As relative density increases to 0.1, both CSL and ISL develop increasingly stable stress profiles with notably enhanced performance. At this higher density, neither lattice exhibits the pronounced clustering phenomena observed in ISL at $\bar{\rho} = 0.05$. The buckling mechanisms, which previously reduced load-bearing capacity, are effectively eliminated, as evidenced by stress-strain curves. This manifests distinctly in each lattice: CSL shows sharply reduced oscillatory behavior; interestingly, ISL transitions from oscillatory patterns to a stabilized, enhanced stress-strain response. This phenomenon is most pronounced at $\bar{\rho} = 0.2$, where both CSL and ISL exhibit stabilized, enhanced stress-strain responses under uniaxial compression (see Figure S7). Although BCC truss lattices demonstrate substantially lower strength and stiffness overall, they exhibit a sharp stress rise under high strain at higher densities due to densification. Despite this localized increase, their strength remains consistently inferior to that of the shell lattices.

To understand the deformation mechanisms responsible for the superior performance of our shell lattices (CSL/ISL) compared to conventional designs, we conducted uniaxial compression simulations on both individual unit cells and $3 \times 3 \times 3$ lattices, applying 30% strain (Fig. 12). We observe that during compression, internal contact behavior evolves in a similar manner within the unit cells of both lattice structures. Our findings show that as compression advances, internal contact occurs within the unit cells of both lattice types. This internal contact acts to constrain deformation transversely (with constraint magnitude linked to the spherical hinge radius), thereby generating a reactive force in the loading direction that enhances strength. It is noteworthy that alongside internal contact, compression also induces protruding shell deformation, arising directly from the presence of oversized spherical hinges. This transition from a normal state to one featuring internal contact allows the designed lattices to achieve a significantly enhanced stress-strain response at a relative density of 0.1, demonstrating strong yield strength and high stress values throughout the nonlinear stage.

The internal contact mechanism observed in the CSL and ISL represents a distinct novelty, seldom encountered in other lattice designs. A key limitation of most lattices at low relative densities is their inability to actively exploit intra-unit cell space to generate beneficial shell contact, thereby failing to constrain deformation effectively. Contact between their constituent materials typically

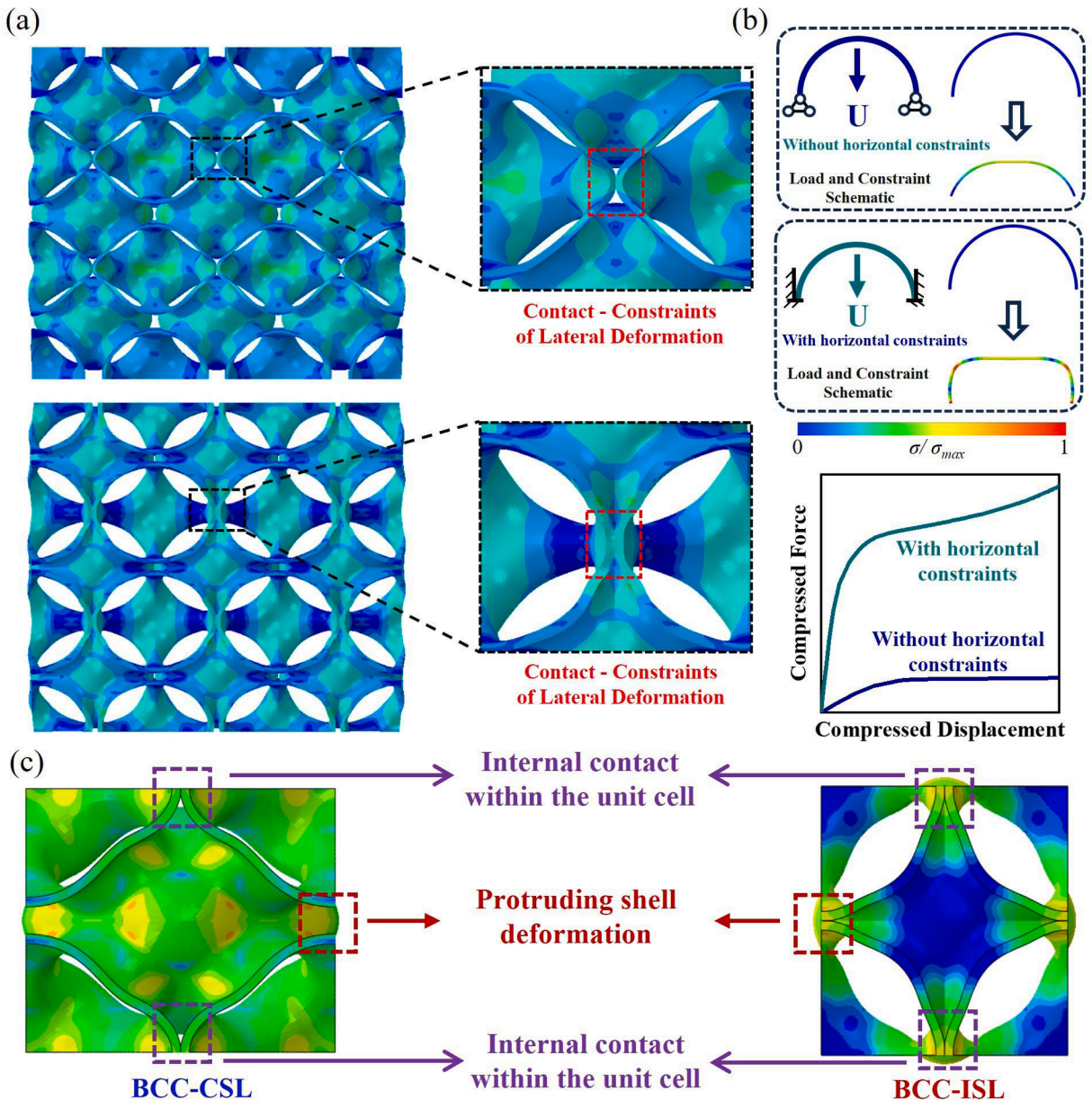

Fig. 12. (a) Schematic of 3×3×3 lattice compression simulation with lateral contact constraints. (b) Deformation comparison of bent beams with/without lateral displacement constraints and resulting reaction forces. (c) Deformed CSL and ISL unit cells at 30% strain.

arises passively, only after substantial densification or severe inter laminar crushing has occurred, by which point its impact on mechanical performance is severely limited. Moreover, lattices pursuing ultra-smooth surfaces develop “Concave shell deformation” under uniaxial compression; their gradual curvature prevents the deformational squeezing necessary for contact initiation. Thus, although achieving potentially higher yield strength and stiffness, these smooth lattices lack the ability to maintain high strength throughout the nonlinear phase (Fig. 12b). Crucially, both “Internal contact within the unit cell” and “Protruding shell deformation” are inherent and active mechanisms within ISL and CSL during compression, as clearly demonstrated in Fig. 12(c). These mechanisms are regularly activated as α and β change. For the criteria, please refer to Note S2, Figure S9, and Figure S10.

For lattice materials, Specific Energy Absorption (SEA) quantifies the energy absorbed per unit mass when the material is deformed to 50% strain under uniaxial compression. SEA is defined as follows:

$$\mathrm{SEA} = \frac{1}{\rho}\int_0^{0.5} \sigma \, d\varepsilon \tag{10}$$

Where ρ is the density of the lattices, σ is the axial stress, and ε is the axial strain.

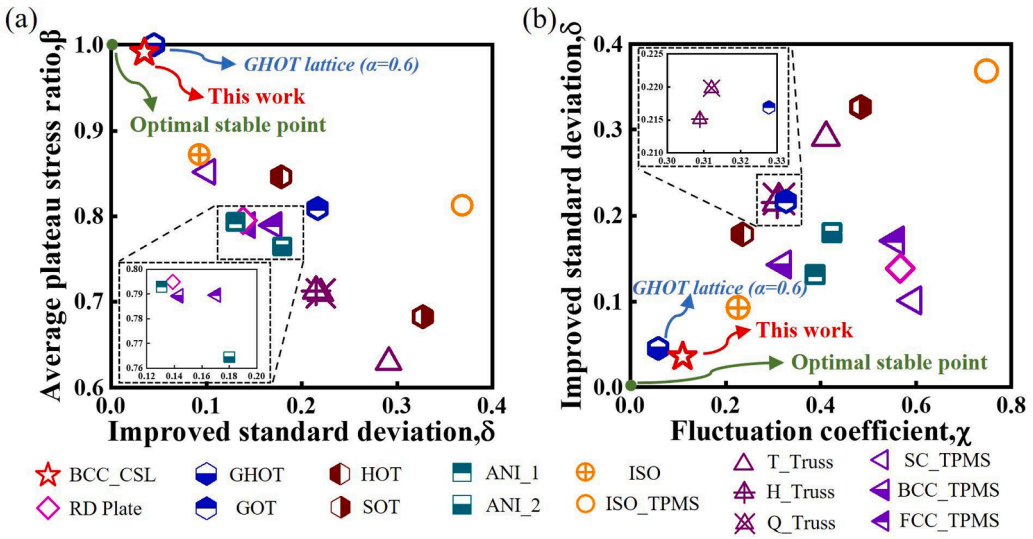

Fig. 13. Evaluation of nonlinear deformation stability: Proposed shell lattices (CSL) versus conventional bending-dominated lattices and stretching-dominated lattices under uniaxial compression (Chen et al., 2024; Zhang et al., 2025, 2023; Duan et al., 2020; Bonatti and Mohr, 2019a,b; Li et al., 2020).

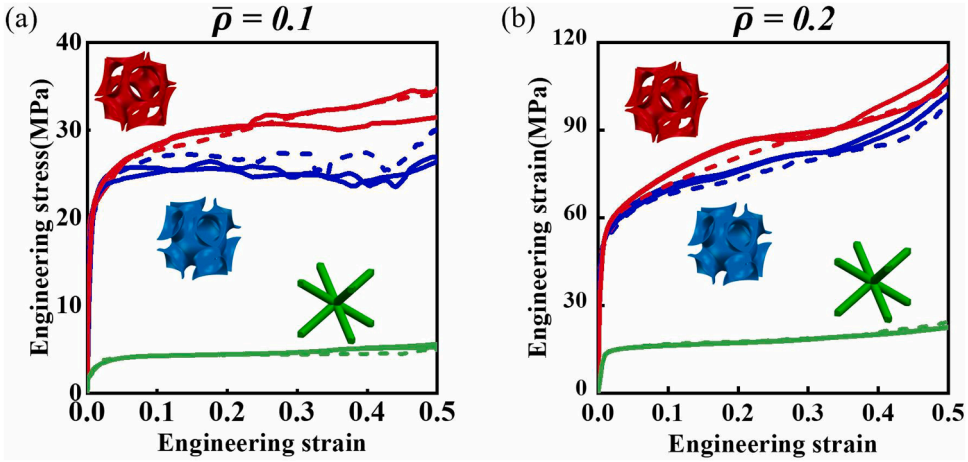

Fig. 14. Simulated and experimental uniaxial compression response of ISL, CSL and BCC truss lattices at relative densities of (a) $\overline{\rho} = 0.1$ and (b) $\overline{\rho} = 0.2$.

Leveraging their enhanced strength in the nonlinear deformation stage, CSL and ISL demonstrate superior energy absorption capabilities. At a relative density of 0.1, for instance, ISL achieves a SEA of 23.2 J/g, which is approximately 7.4 times higher than the 3.13 J/g exhibited by conventional BCC solid truss lattices.

5.4. Evaluation of nonlinear stability for lattice materials

When evaluating the stability of the nonlinear stress-strain curve of lattice materials, three main parameters are used: (i) average plateau stress ratio; (ii) improved standard deviation; and (iii) improved standard deviation. The respective formulas are as follows (Zhang et al., 2025):

$$\beta = \frac{\overline{\sigma}_{ave}}{\sigma_{peak}} \tag{11}$$

Where,

$$\overline{\sigma}_{\text{ave}} = \frac{\sum_{n=1}^{i-1}\left[(\varepsilon_{n+1}-\varepsilon_n)(\sigma_{n+1}+\sigma_n)\right]}{2(\varepsilon_i-\varepsilon_1)} \tag{12}$$

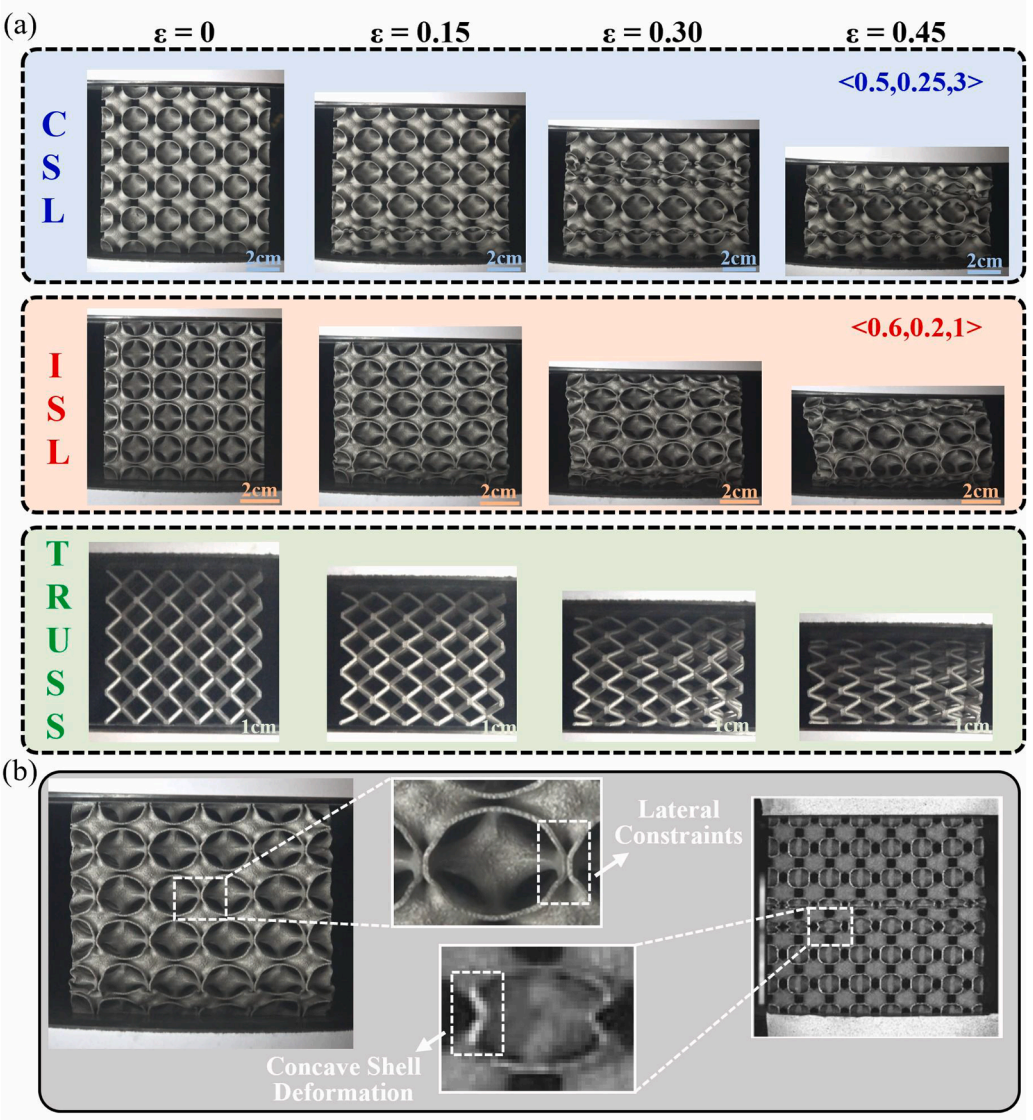

Fig. 15. (a) Representative deformation frames of shell (ISL/CSL), and truss lattices at a relative density of 0.1 under discrete compressive strains. (b) Mechanism underlying the enhanced mechanical properties of the designed shell lattices compared to existing types (Bonatti and Mohr, 2019b).

Where, $\overline{\sigma}_{ave}$ represents the average platform stress, σ_{peak} is the initial peak stress, and i represents the number of data points on the stress-strain curve.

$$\delta = \sqrt{\frac{1}{i}\sum_{n=1}^{i}\left(\frac{\sigma_n}{\overline{\sigma}_{ave}} - 1\right)^2} \tag{13}$$

$$\chi = 1 - \left[1 - \sum_{n=1}^{i-1}\left(\frac{\varepsilon_{n+1} - \varepsilon_n}{\varepsilon_i - \varepsilon_1}\frac{|\frac{\Delta\sigma}{\Delta\varepsilon}|_n}{|\frac{\Delta\sigma}{\Delta\varepsilon}|_{max}}\right)\right]\beta \tag{14}$$

Where, $|\frac{\Delta\sigma}{\Delta\varepsilon}|_n$ is the absolute slope between two adjacent points, and$|\frac{\Delta\sigma}{\Delta\varepsilon}|_{\max}$ is the maximum slope gradient of any two adjacent points in all comparison curves at the same relative density.

Using the above equations, we calculate $\beta_{ISL<0.6,0.2,1>} = 1.20$. This value satisfies the criterion for enhanced stress-strain behavior ($\beta > 1$), confirming the transition from fluctuating to stabilized strengthening at low relative density. Following this framework, we compared $CSL < 0.5, 0.25, 3 >$ ($\overline{\rho} = 0.1$) with other lattices at identical relative density (See Fig. 13). Stability was assessed via $\delta - \beta$ and $\chi - \delta$ curves, where ideal stability corresponds to coordinates (1,0) and (0,0), respectively marked in the figure. Among all lattices, CSL achieves the closest δ-value to optimal and exhibits overall stability comparable to GHOT. Crucially, CSL demonstrates superior

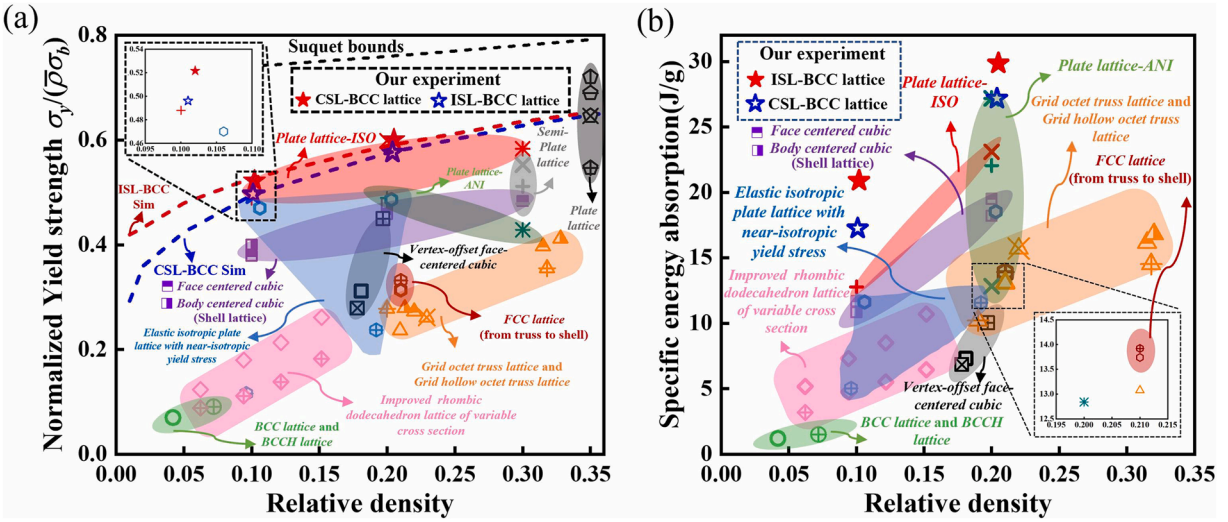

Fig. 16. Performance comparison on Ashby plots: Proposed lattices versus state of the art energy-absorbing lattices in (a) yield strength and (b) specific energy absorption (SEA) (Zhang et al., 2025, 2023; Bonatti and Mohr, 2019b; Wu et al., 2023; Bonatti and Mohr, 2017; Tancogne-Dejean et al., 2016; Li et al., 2020; Cao et al., 2018; Wang et al., 2025, 2021b).

stability performance relative to other conventional lattices which attributable to its contact-enhancing design. This structural strategy significantly improves compressive response stability and enhances energy absorption efficiency at low relative densities.

5.5. Comparison between experiment and simulation

Fig. 14 and 15 summarizes the compressive stress-strain behavior and associated deformation patterns (See Movie.S1-S6) for all samples, comparing experimental (two solid lines) and simulated (dashed lines) results. Key metrics, including elastic modulus, yield strength, large nonlinear response, and $SEA_{50\%}$, exhibit a strong correlation between experiment and simulation. This agreement persists even though the simulations model a smaller ($3\times3\times3$ unit) domain than the experimental ($5\times5\times5$ unit) samples, corroborating findings by Colin Bonatti et al. and demonstrating mutual method validation (Bonatti and Mohr, 2017).

At a relative density of 0.1, ISL shows pronounced stress enhancement during the nonlinear stage, while CSL exhibits stress stabilization despite its smoother local geometry. In contrast, BCC truss lattices deform uniformly but underperform in yield strength, elastic modulus, and specific energy absorption compared to the shell lattices developed here. At higher relative densities, CSL transitions to stress-enhancing behavior in the nonlinear stage, mirroring the response of ISL. Critically, BCC lattices remain mechanically inferior to both shell architectures.

Unlike TPMS lattices exhibiting invaginated buckling, ISL develops convex deformation patterns under compression (Fig. 14d). This morphology triggers inter-shell contact with increasing strain, generating transverse constraints that produce a stress-hardening response. These observations validate our simulation-predicted mechanism, confirming the design rationale.

To benchmark ISL and CSL against established energy-absorbing architectures, we compare their density-dependent performance with leading truss, tube, shell, and plate lattices, as illustrated in Fig. 16. The proposed lattices demonstrate exceptional SEA and normalized yield strength at low-to-moderate relative densities. Notably, their SEA significantly outperforms shell/plate lattices while exhibiting superior stability, achieving nearly twice the SEA of conventional TPMS-like shell lattices at a relative density of 0.1. Experimental and simulated yield strength show strong agreement, with normalized values surpassing all benchmarked lattices except for some anisotropic closed-form plate lattices at high relative density (Liu, 2021). However, when considering the fabrication challenges and nonlinear instability of those plate lattices, our shell lattice delivers a more consistent and robust performance envelope. This performance originates from a novel design principle: contact-induced transverse constraints during large-strain compression provide supplemental resistance, particularly enhanced at low relative density. The synergy of tunable properties and high mechanical efficiency establishes the proposed shell lattices as premier candidates for load-bearing energy absorbers.

6. Conclusion

We propose an innovative parametric design methodology for three-dimensional shell lattice metamaterials that significantly enhances mechanical performance while maintaining nonlinear stability at low relative densities as low as 0.1. Notably, it also delivers a more stable and enhanced nonlinear stress-strain response at a density of 0.05 than other lattices specifically engineered for such stability. This is achieved by combining stretching-dominated behavior with contact-enhancement mechanisms through elliptical-curve-based node connections and tri-parameter (α, β, γ) modulation. Numerical simulations and experimental tests characterize the elastic properties and large-deformation compression response of the proposed CSL, ISL, and benchmark truss lattices. Results

demonstrate that the proposed shell lattices achieve peak Young's modulus and yield strength near $\alpha = 0.6$, while variations in β and γ have negligible impact. The distribution of the shear modulus, in contrast, is sensitive to changes in α and β, but unaffected by γ. The parameter γ itself determines the geometric configuration, classifying lattices as either ISL or CSL. Elastic isotropy can be achieved via parameter optimization, while broad tenability allows for customized anisotropic elastic responses.

Across relative densities of 0.01-0.5, CSL and ISL lattices exceed traditional truss and shell lattices in Young's modulus, yield strength, energy absorption, and nonlinear stability. At a relative density of 0.1, they demonstrate substantial improvements over conventional BCC truss lattices: 2460% higher Young's modulus, 572% greater yield strength, and 641% increased energy absorption. Notably, their SEA reaches nearly twice that of conventional TPMS-like shell lattices. These enhancements stem from internal contact mechanisms that stabilize post-buckling behavior, producing consistent or enhanced stress-strain responses. This methodology thus overcomes limitations of stretching-dominated lattices at low densities, paving a new way for designing lightweight load-bearing structures, energy absorbers, and multifunctional metamaterials.

CRediT authorship contribution statement

Peijie Zhang: Writing – original draft, Software, Methodology, Investigation, Formal analysis, Data curation, Conceptualization; **Xueyan Chen:** Writing – review & editing, Validation, Supervision, Resources, Methodology, Investigation, Funding acquisition, Conceptualization; **Penghui Yu:** Formal analysis, Data curation; **Kun Zhao:** Visualization, Validation, Formal analysis, Data curation; **Hang Yin:** Visualization, Validation, Formal analysis; **Changguo Wang:** Writing - review & editing, Visualization, Validation; **Huifeng Tan:** Writing – review & editing, Visualization, Validation, Supervision; **Muamer Kadic:** Writing – review & editing, Visualization, Validation, Supervision, Conceptualization.

Supplementary material

Supplementary material associated with this article can be found in the online version at 10.1016/j.jmps.2025.106467

Data availability

Data will be made available on request.

Declaration of competing interest

The authors declare that they have no known competing financial interests or personal relationships that could have appeared to influence the work reported in this paper.

Acknowledgments

This work was supported by the National Natural Science Foundation of China under Grant No. 12202118, Science Foundation of National Key Laboratory of Science and Technology on Advanced Composites in Special Environments and China Postdoctoral Science Foundation (2025T181142 and 2023M730865).

References

Abbasi, A., Chen, T., Aymon, B. F.G., Reis, P.M., 2024. Leveraging the snap buckling of bistable magnetic shells to design a refreshable braille dot. Adv. Mater. Technol. 9 (3), 2301344.
Baishya, M.J., Muthu, N., Khanikar, P., 2024. In pursuit of a high-performance mechanical metamaterial: simple-cubic-octahedral plate lattice. Int. J. Mech. Sci. 272, 109189.
Bonatti, C., Mohr, D., 2017. Large deformation response of additively-manufactured FCC metamaterials: from octet truss lattices towards continuous shell mesostructures. Int. J. Plast. 92, 122–147.
Bonatti, C., Mohr, D., 2019a. Mechanical performance of additively-manufactured anisotropic and isotropic smooth shell-lattice materials: simulations & experiments. J. Mech. Phys. Solids 122, 1–26.
Bonatti, C., Mohr, D., 2019b. Smooth-shell metamaterials of cubic symmetry: anisotropic elasticity, yield strength and specific energy absorption. Acta Mater. 164, 301–321.
Cao, X., Duan, S., Liang, J., Wen, W., Fang, D., 2018. Mechanical properties of an improved 3d-printed rhombic dodecahedron stainless steel lattice structure of variable cross section. Int. J. Mech. Sci. 145, 53–63.
Chen, T., Pauly, M., Reis, P.M., 2021. A reprogrammable mechanical metamaterial with stable memory. Nature 589 (7842), 386–390.
Chen, X., Ji, Q., Wei, J., Tan, H., Yu, J., Zhang, P., Laude, V., Kadic, M., 2020. Light-weight shell-lattice metamaterials for mechanical shock absorption. Int. J. Mech. Sci. 169, 105288.
Chen, X., Moughames, J., Ji, Q., Martínez, J. A.I., Tan, H., Ulliac, G., Laude, V., Kadic, M., 2022. 3D lightweight mechanical metamaterial with nearly isotropic inelastic large deformation response. J. Mech. Phys. Solids 169, 105057.
Chen, X., Yu, P., Ma, H., Zhang, P., Ding, C., Liu, S., Zhang, X., Tan, H., 2024. A class of elastic isotropic plate lattice materials with near-isotropic yield stress. Acta Mater. 276, 120085.
Deshpande, V.S., Ashby, M.F., Fleck, N.A., 2001a. Foam topology: bending versus stretching dominated architectures. Acta Mater. 49 (6), 1035–1040.
Deshpande, V.S., Fleck, N.A., Ashby, M.F., 2001b. Effective properties of the octet-truss lattice material. J. Mech. Phys. Solids 49 (8), 1747–1769.
Duan, S., Wen, W., Fang, D., 2020. Additively-manufactured anisotropic and isotropic 3d plate-lattice materials for enhanced mechanical performance: simulations & experiments. Acta Mater. 199, 397–412.
Dudek, K.K., Kadic, M., Coulais, C., Bertoldi, K., 2025a. Shape-morphing metamaterials. Nat. Rev. Mater. 1–16.

Dudek, K.K., Martínez, J.A.I., Hirsinger, L., Kadic, M., Devel, M., 2025b. Active magneto-mechanical metamaterial with the wave transmission and poisson's ratio controlled via the magnetic field. J. Sound Vib. 595, 118784.
Eberl, C., Thompson, R., Gianola, D., Bundschuh, S., 2006. Digital image correlation and tracking with matlab. Matlab Central file exchange.
Guo, X., Ding, J., Li, X., Qu, S., Song, X., Fuh, J. Y.H., Lu, W.F., Zhai, W., 2022. Enhancement in the mechanical behaviour of a schwarz primitive periodic minimal surface lattice structure design. Int. J. Mech. Sci. 216, 106977.
Hamzehei, R., Bodaghi, M., Iglesias Martinez, J.A., Ji, Q., Ulliac, G., Kadic, M., Wang, C., Zolfagharian, A., Wu, N., 2023. Parrot beak-inspired metamaterials with friction and interlocking mechanisms 3d/4d printed in micro and macro scales for supreme energy absorption/dissipation. Adv. Eng. Mater. 25 (11), 2201842.
Han, L., Che, S., 2018. An overview of materials with triply periodic minimal surfaces and related geometry: from biological structures to self-assembled systems. Adv. Mater. 30 (17), 1705708.
Han, S.C., Lee, J.W., Kang, K., 2015. A new type of low density material: shellular. Adv. Mater. Weinheim 27 (37), 5506–5511.
Jeong, Y.C., Han, S.C., Wu, C.H., Kang, K., 2024. A micro-architectured material as a pressure vessel for green mobility. Nat. Commun. 15 (1), 353.
Jiang, B., Chen, X., Yu, J., Zhao, Y., Xie, Z., Tan, H., 2022. Energy-absorbing properties of thin-walled square tubes filled with hollow spheres. Thin-Walled Struct.s 180, 109765.
Jiménez, F.L., Upadhyaya, P., Liljenhjerte, J., Reis, P.M., Kumar, S., 2016. Soft optical composites for tunable transmittance. Extreme Mech. Lett. 9, 297–303.
Jin, Y., Torrent, D., Rouhani, B.D., He, L., Xiang, Y., Xuan, F.-Z., Gu, Z., Xue, H., Zhu, J., Wu, Q., et al., 2025. The 2024 phononic crystals roadmap. J. Phys. D Appl. Phys. 58 (11), 113001.
Kladovasilakis, N., Tsongas, K., Kostavelis, I., Tzovaras, D., Tzetzis, D., 2022. Effective mechanical properties of additive manufactured strut-lattice structures: experimental and finite element study. Adv. Eng. Mater. 24 (3), 2100879.
Lan, T., Tran, P., Nguyen, K.T., Xuan, H.N., Thai, D.-K., 2025. 3D printed functionally graded hollow lattice structures: multidimensional design for large deformation. Compos. Struct. , 119490.
Li, C., Lei, H., Liu, Y., Zhang, X., Xiong, J., Zhou, H., Fang, D., 2018. Crushing behavior of multi-layer metal lattice panel fabricated by selective laser melting. Int. J. Mech. Sci. 145, 389–399.
Li, C., Lei, H., Zhang, Z., Zhang, X., Zhou, H., Wang, P., Fang, D., 2020. Architecture design of periodic truss-lattice cells for additive manufacturing. Addit. Manuf. 34, 101172.
Li, R., Ma, W. W.S., Niu, T., Liu, H., Ding, J., Song, X., 2025. Stiffness and strength enhancement of hierarchical TPMS-based shell lattices via inter-level conformal design. Addit. Manuf. , 104802.
Li, S., Wongsto, A., 2004. Unit cells for micromechanical analyses of particle-reinforced composites. Mech. Mater. 36 (7), 543–572.
Li, T., Jarrar, F., Al-Rub, R.A., Cantwell, W., 2021a. Additive manufactured semi-plate lattice materials with high stiffness, strength and toughness. Int. J. Solids Struct. 230, 111153.
Li, X., Yu, X., Chua, J.W., Lee, H.P., Ding, J., Zhai, W., 2021b. Microlattice metamaterials with simultaneous superior acoustic and mechanical energy absorption. Small 17 (24), 2100336.
Li, X., Yu, X., Zhai, W., 2021c. Additively manufactured deformation-recoverable and broadband sound-absorbing microlattice inspired by the concept of traditional perforated panels. Adv. Mater. 33 (44), 2104552.
Liu, C., Ni, R., Ji, K., Zhao, A., Sun, X., Wu, H., 2024. Improving mechanical properties of lattice structures using nonuniform hollow struts. Int. J. Mech. Sci. 283, 109674.
Liu, H., Chng, Z. X.C., Wang, G., Ng, B.F., 2021. Crashworthiness improvements of multi-cell thin-walled tubes through lattice structure enhancements. Int. J. Mech. Sci. 210, 106731.
Liu, Y., 2021. Mechanical properties of a new type of plate–lattice structures. Int. J. Mech. Sci. 192, 106141.
López Jiménez, F., Kumar, S., Reis, P.M., 2016. Soft color composites with tunable optical transmittance. Adv. Opt. Mater. 4 (4), 620–626.
Mahbod, M., Asgari, M., Mittelstedt, C., 2020. Architected functionally graded porous lattice structures for optimized elastic-plastic behavior. Proceedings of the Institution of Mechanical Engineers, Part L: Journal of Materials: Design and Applications 234 (8), 1099–1116.
Meyer, P.P., Tancogne-Dejean, T., Mohr, D., 2024. Non-symmetric plate-lattices: recurrent neural network-based design of optimal metamaterials. Acta Mater. 278, 120246.
Meyers, M.A., Chawla, K.K., 2008. Mechanical behavior of materials. Cambridge university press.
Meza, L.R., Das, S., Greer, J.R., 2014. Strong, lightweight, and recoverable three-dimensional ceramic nanolattices. Science 345 (6202), 1322–1326.
Milton, G., Briane, M., Harutyunyan, D., 2017. On the possible effective elasticity tensors of 2-dimensional and 3-dimensional printed materials. Math. Mech. Complex Syst. 5 (1), 41–94.
Noronha, J., Dash, J., Leary, M., Downing, D., Kyriakou, E., Brandt, M., Qian, M., 2023. Node-reinforced hollow-strut metal lattice materials for higher strength. Scr. Mater. 234, 115547.
Poincloux, S., Vallat, C., Chen, T., Sano, T.G., Reis, P.M., 2023. Indentation and stability of woven domes. Extreme Mech. Lett. 59, 101968.
Portela, C.M., Greer, J.R., Kochmann, D.M., 2018. Impact of node geometry on the effective stiffness of non-slender three-dimensional truss lattice architectures. Extreme Mech. Lett. 22, 138–148.
Queheillalt, D.T., Wadley, H. N.G., 2005a. Cellular metal lattices with hollow trusses. Acta Mater. 53 (2), 303–313.
Queheillalt, D.T., Wadley, H. N.G., 2005b. Pyramidal lattice truss structures with hollow trusses. Mater. Sci. Eng.: A 397 (1–2), 132–137.
Schaedler, T.A., Jacobsen, A.J., Torrents, A., Sorensen, A.E., Lian, J., Greer, J.R., Valdevit, L., Carter, W.B., 2011. Ultralight metallic microlattices. Science 334 (6058), 962–965.
Shu, Z., Zhao, K., Li, H., Gao, L., 2025. Multi-scale topology optimization for graded hollow lattice structures with variable wall thickness. Thin-Walled Struct. 213, 113274.
Song, J., Zhou, W., Wang, Y., Fan, R., Wang, Y., Chen, J., Lu, Y., Li, L., 2019. Octet-truss cellular materials for improved mechanical properties and specific energy absorption. Mater. Des. 173, 107773.
Song, Y., Chen, Z., Wei, T., Ge, C., Cheng, Y., Liu, M., Jia, Q., 2024. Mechanical performance of bamboo-inspired tapered hollow strut lattice structures fabricated by laser powder bed fusion (LPBF). Adv. Manuf. 1 (3), 1–21.
Syrlybayev, D., Yankin, A., Perveen, A., Talamona, D., 2024. Slm-printed lattice structures with tapered vertical struts: design, simulation and experimentation. Manuf. Lett. 41, 803–809.
Tan, X., Cao, B., Liu, W., Ji, C., Wang, B., Li, S., 2024a. Odd mechanical metamaterials with simultaneously expanding or contracting under both compression and tension. Thin-Walled Struct. 203, 112225.
Tan, X., Cao, B., Liu, X., Zhu, S., Chen, S., Kadic, M., Wang, B., 2024b. Negative stiffness mechanical metamaterials: a review. Smart Mater. Struct. .
Tan, X., Martínez, J. A.I., Ulliac, G., Wang, B., Wu, L., Moughames, J., Raschetti, M., Laude, V., Kadic, M., 2022. Single-step-lithography micro-stepper based on frictional contact and chiral metamaterial. Small 18 (28), 2202128.
Tan, X., Zhu, S., Wang, B., Kadic, M., 2024c. Tuning negative stiffness mechanical metamaterial's snap-through behavior with a series-connected spring. Eur. J. Mech.-A/Solids 107, 105382.
Tancogne-Dejean, T., Diamantopoulou, M., Gorji, M.B., Bonatti, C., Mohr, D., 2018. 3D plate-lattices: an emerging class of low-density metamaterial exhibiting optimal isotropic stiffness. Adv. Mater. 30 (45), 1803334.
Tancogne-Dejean, T., Li, X., Diamantopoulou, M., Roth, C.C., Mohr, D., 2019. High strain rate response of additively-manufactured plate-lattices: experiments and modeling. J. Dyn. Behav. Mater. 5 (3), 361–375.
Tancogne-Dejean, T., Mohr, D., 2018. Elastically-isotropic elementary cubic lattices composed of tailored hollow beams. Extreme Mech. Lett. 22, 13–18.
Tancogne-Dejean, T., Spierings, A.B., Mohr, D., 2016. Additively-manufactured metallic micro-lattice materials for high specific energy absorption under static and dynamic loading. Acta Mater. 116, 14–28.

Wang, P., Guo, J., Yuan, Y., Li, C., Wang, Y., Guang, M., Yan, J., Liu, W., Sun, Z., 2025. Bio-inspired vertex-offset lattice metamaterials with enhanced stress stability and energy absorption. Thin-Walled Struct. 210, 113060.
Wang, Y., Liu, F., Zhang, X., Zhang, K., Wang, X., Gan, D., Yang, B., 2021a. Cell-size graded sandwich enhances additive manufacturing fidelity and energy absorption. Int. J. Mech. Sci. 211, 106798.
Wang, Z., Zhou, Y., Wang, X., Wei, K., 2021b. Compression behavior of strut-reinforced hierarchical lattice–experiment and simulation. Int. J. Mech. Sci. 210, 106749.
Wu, J., Zhang, Y., Yang, F., Jiang, F., Xu, X., Tan, Y., Su, L., 2023. A hybrid architectural metamaterial combing plate lattice and hollow-truss lattice with advanced mechanical performances. Addit. Manuf. 76, 103764.
Yan, S., Liu, W., Tan, X., Meng, Z., Luo, W., Jin, H., Wen, Y., Sun, J., Wu, L., Zhou, J., 2024a. Bio-inspired mechanical metamaterial with ultrahigh load-bearing capacity for energy dissipation. Mater. Today 77, 11–18.
Yan, S., Wu, L., Meng, Z., Tan, X., Liu, W., Wen, Y., Sun, J., Tian, X., Zhou, J., 2024b. Double-strip metamaterial for vibration isolation and shock attenuation. Int. J. Mech. Sci. 282, 109686.
Yin, S., Guo, W., Wang, H., Huang, Y., Yang, R., Hu, Z., Chen, D., Xu, J., Ritchie, R.O., 2021. Strong and tough bioinspired additive-manufactured dual-phase mechanical metamaterial composites. J. Mech. Phys. Solids 149, 104341.
Yu, P., Zhang, P., Ji, Q., Yang, F., Tan, X., Chen, X., Tan, H., Laude, V., Kadic, M., 2024. A multi-step auxetic metamaterial with instability regulation. Int. J. Solids Struct. 305, 113040.
Zhang, L., Feih, S., Daynes, S., Chang, S., Wang, M.Y., Wei, J., Lu, W.F., 2018. Energy absorption characteristics of metallic triply periodic minimal surface sheet structures under compressive loading. Addit. Manuf. 23, 505–515.
Zhang, P., Chen, X., Yu, P., Zhao, K., Ma, H., Liu, S., Tan, H., Laude, V., Kadic, M., 2025. Grid hollow octet truss lattices that are stable at low relative density. J. Mech. Phys. Solids 197, 106068.
Zhang, P., Yu, P., Zhang, R., Chen, X., Tan, H., 2023. Grid octet truss lattice materials for energy absorption. Int. J. Mech. Sci. 259, 108616.
Zhao, J., Ritchie, R.O., Xiong, J., 2025. High-performance programmable combinatorial lattice materials. J. Mech. Phys. Solids , 106351.
Zhao, M., Zhang, D.Z., Li, Z., Zhang, T., Zhou, H., Ren, Z., 2022. Design, mechanical properties, and optimization of BCC lattice structures with taper struts. Compos. Struct. 295, 115830.
Zhu, S., Chen, H., Yang, X., Tan, L., Jin, S., Chen, L., Liu, T., Tan, X., Wang, L., Wang, B., et al., 2024. Rubik's cube as in-situ programmable matter and a reconfigurable mechanical metamaterial. Sci. China Technol. Sci. 67 (10), 3221–3234.